JM PAPERS

High-fidelity simulations of microramp-controlled shock wave/boundary layer interaction

G. Della Posta[1,†]**, E. Martelli**[2]**, F. Salvadore**[3] **and M. Bernardini**[1]

[1]Department of Mechanical and Aerospace Engineering, Sapienza University of Rome, via Eudossiana 18, 00184 Rome, Italy

[2]Department of Mechanical and Aerospace Engineering, Politecnico di Torino, Corso Duca degli Abruzzi 24, 10129 Torino, Italy

[3]HPC Department, CINECA, via dei Tizii 6/B, 00185 Rome, Italy

Microvortex generators (MVGs) are a promising solution to control shock wave/turbulent boundary layer interactions (SBLIs), especially in supersonic inlets. In this study, we examine the effects of a microramp vortex generator on an SBLI generated by an oblique shock wave and a turbulent boundary layer using direct numerical simulations (DNSs). Two cases, with and without the presence of a microramp, are compared in terms of their mean and unsteady flow features at free-stream Mach number equal to 2 and friction Reynolds number at the inviscid shock impingement equal to 600. The long integration period allows us to assess how microramps affect the typical low-frequency unsteadiness observed in SBLIs, and the data generated may serve as a reference for simulations of lower fidelity or reduced order models. The analysis shows that the three-dimensional microramp wake alters the interaction region dramatically, inducing a significant spanwise modulation and topology change of the separation. For example, tornado-like structures redistribute the flow in both the spanwise and wall-normal directions inside the recirculation region. The increase in momentum close to the wall by the ramp vortices effectively delays the onset of the separation and, thus, the separation length, but at the same time leads to a significant increase in the intensity of the wall-pressure fluctuations. We then characterise the mutual interaction between the arch-like vortices around the ramp wake and the SBLI. The specific spanwise vorticity shows that these vortices follow the edge of the separation and their intensity, apart from mean compressibility effects, is not affected by the shocks. The shocks, instead, are deformed in shape by the periodic impingement of the vortices, although the spectral analysis did not reveal any significant trace of their

† Email address for correspondence: giacomo.dellaposta@uniroma1.it

shedding frequency in the separation region. These Kelvin–Helmholtz vortices, however, may be relevant in the closure of the separation bubble. Fourier analysis also shows a constant increase, in both value and magnitude, in the low-frequency peak all along the span, suggesting that the motion of the separation shock remains coherent while being disturbed by the arch-like vortices and oscillating at a higher frequency in absolute terms.

Key words: compressible boundary layers, shock waves

1. Introduction

It is widely recognised that the interaction between shock waves and boundary layers poses significant challenges for aerospace systems. Increased thermomechanical loads, shock-induced separation, amplified pressure losses, and intermittent, low-frequency flow unsteadiness that may interact with structures represent only some of the possible hazardous effects shock wave/boundary layer interaction (SBLI) may cause. For this reason, significant research efforts during the last decade have focused on possible control solutions aiming at cancelling, or at least mitigating, some of the detrimental consequences of SBLI.

Among the proposed control remedies, microvortex generators (MVGs) (and, in particular, microramps) are promising passive devices, smaller than the boundary layer thickness, that generate a system of trailing vortices energising the boundary layer (McCormick 1993; Anderson, Tinapple & Surber 2006). Such vortices bring high-momentum fluid closer to the wall, which makes the velocity profile fuller and hence more resistant to the separation induced by the following shock wave impingement. Researchers have demonstrated that MVGs have the potential to reduce shock-induced separation, even if some aspects of the flow generated are still unclear due to the complexity of the new interaction taking place between the shock and the incoming flow (Lu, Li & Liu 2012; Panaras & Lu 2015; Titchener & Babinsky 2015).

Several studies have first clarified the organisation of the wake behind a microramp immersed into a turbulent boundary layer. Both experimental (Sun *et al.* 2012) and numerical (Lee & Loth 2009) results regarding the mean flow field revealed a low-momentum region in the wake, associated with the so-called primary vortex pair. Indeed, the two vortices developing at the sides of the MVG converge at the trailing edge and then proceed approximately in parallel in the streamwise direction. In addition to adding momentum to the region close to the wall, the primary vortices are associated with the presence of secondary vortices at the bottom and top corners at the side walls of the ramp and mutually induce a lift-up at the symmetry plane that gradually pushes the wake far from the wall after the ramp (Babinsky, Li & Ford 2009; Lu *et al.* 2010). The vortex pair decays slowly and continues to energise the boundary layer even far downstream of the main interaction, when SBLI is present (Ghosh, Choi & Edwards 2008). The differences in the mean wake development have been quantified for several geometrical and flow parameters, such as the relative height of the ramp (Babinsky *et al.* 2009; Giepman *et al.* 2015; Tambe, Schrijer & van Oudheusden 2021), the Reynolds number (Della Posta *et al.* 2023; Salvadore *et al.* 2023) and the Mach number (Giepman *et al.* 2016; Della Posta *et al.* 2023*a*).

The instantaneous flow structure is, instead, more controversial. Researchers agree about the periodic shedding from the ramp of almost-toroidal vortical structures quickly developing around the low-momentum region as a consequence of Kelvin–Helmholtz (K–H) instability, but they debate on their precise nature. On one side, K–H vortices are

seen as closed vortex rings with connected filaments in the bottom part (Li & Liu 2010). On the other side, it is assumed that the legs of the top arch are not connected and, instead, become parallel to the wall in their bottom part, thus forming hairpin vortices (Blinde *et al.* 2009). Through the analysis of direct numerical simulation (DNS) results in terms of mean vorticity field and characteristic-based dynamic mode decomposition (DMD), Della Posta *et al.* (2023*a*) characterised the properties of the top arch-like vortical structures for a range of Mach numbers, but, as in Bo *et al.* (2012), did not detect the bottom vortex cores that should be associated with the closure of the vortex rings at the symmetry plane. Results thus suggest that wall turbulence dominates over the K–H instability of the bottom shear layer and prevents the formation of closed vortex rings even after a large distance from the ramp, where the wake is further from the wall because of the lift-up from the primary vortex pair. Moreover, the analysis of the near wake in Della Posta *et al.* (2023) highlighted a strong connection between the vortical structures around the wake and those inside of it close to the ramp trailing edge, as a consequence of the internal convolution of the primary vortices at the sides of the ramp. Various conceptual models have been proposed describing the evolution of the instantaneous vortical organisation (Blinde *et al.* 2009; Bo *et al.* 2012; Sun *et al.* 2014; Della Posta *et al.* 2023) but a clear and definite understanding is still missing.

The introduction in the field of a shock wave impinging on the perturbed boundary layer complicates further the scenario. The first effect of MVGs on SBLI is the overall reduction of the extent of the separation region, observed in both experiments (Babinsky *et al.* 2009; Blinde *et al.* 2009; Giepman, Schrijer & van Oudheusden 2014) and simulations (Grébert *et al.* 2018; Sun *et al.* 2019). The shock foot is generally displaced downstream, and the separation length is reduced compared with the uncontrolled case. In some experimental works, reversed flow even disappears at some spanwise sections (Giepman *et al.* 2014), although reduced resolution close to the wall affects the results. In general, however, a notable difference is that the separation is modulated by MVGs in the spanwise direction, with alternating regions of reduced and increased skin friction. Indeed, the microramp wake induces a strong three-dimensionality of the flow impacting the shock wake that alters completely the topology of the interaction region compared with the traditional two-dimensional (2-D) SBLI. In addition to presenting the spanwise modulation of the separation length, oil-flow visualisations in Babinsky *et al.* (2009) and skin-friction lines based on large eddy simulation (LES) results in Grébert *et al.* (2023) agree with reporting the formation of tornado-like structures lifting the flow from the wall inside the recirculation bubble and transporting it downstream. In particular, the numerical results of Grébert *et al.* (2023) showed that different regions in the span upstream of the interaction contribute differently to the feeding of the separation and that the separation bubble is mostly fed by the flow coming from the sides of the ramp wake. However, understanding if and how these tornado-like structures have an active role in enhancing or attenuating the separation is not straightforward.

Another relevant effect is the periodic disruption of the shock surface due to the arch-like vortices shed by the microramp, first observed in the implicit large eddy simulation (ILES) results of Li & Liu (2010). When impacting the separation region, the primary vortex pair from the ramp and the arch-like vortices around it are mildly affected by the shocks and remain on top of the separation region, thus initially rising and later descending towards the wall after the reflected shock. Yan *et al.* (2013) showed that baroclinic sources of vorticity are negligible and that the interaction between the shocks and the arch-like vortices does not influence the structure of the latter much, also confirmed by Dong *et al.* (2018). The authors thus suggest that the vortices around the microramp wake keep their shapes and vorticity magnitude and travel undisturbed as the shock is

absent. Hence, arch-like vortices seem to be unaffected by shocks, although the shocks are affected by the arch-like vortices, as they generate periodic 'bumps' in the separation shock surface.

In addition, MVGs have an impact on the typical low-frequency unsteadiness associated with SBLI as well. As a matter of fact, MVGs influence all the mechanisms that have been hypothesised to determine and affect this phenomenon. On the one hand, MVGs change dramatically the flow upstream of the interaction, altering the effective thickness of the incoming boundary layer, increasing the anisotropy of the incoming turbulence, and altering the structure of the typical low-speed streaks colliding with the shocks (Lee *et al.* 2010; Bo *et al.* 2012; Salvadore *et al.* 2023), and thus potentially influencing the upstream mechanism proposed by Ganapathisubramani, Clemens & Dolling (2009). On the other hand, if downstream mechanisms are considered: the wake of the microramps completely alters the shape of the separation bubble and thus may affect potential feedback mechanisms such as those proposed by Pirozzoli & Grasso (2006) and Adler & Gaitonde (2018); the additional transfer of momentum towards the wall from the primary vortex pair and the change in the topology of the separation region may affect the mass balance and the properties of fluid entrainment in the mixing layer generated downstream of the separation shock, which is central in the model of Piponniau *et al.* (2009); the change in the shape of the bubble and the vortex pair surviving even after the separation may interfere with the Görtler vortices developing within the separation region and at reattachment observed in Priebe *et al.* (2016) and Pasquariello, Hickel & Adams (2017).

Based on the variance of the shock foot position, Giepman *et al.* (2014) observed that the spanwise modulation of the separation bubble has a beneficial effect on the reflected shock unsteadiness. This observation is also confirmed by the spectral analysis of the wall pressure from the LES results in Grébert *et al.* (2018, 2023), which shows a slight increase in the dominant peak frequency of the shock unsteadiness when averaging wall-pressure spectra in the spanwise direction. However, as in the case of the separation, considerable differences are present at different spanwise sections, although there does not seem to be a trace of the arch-like shedding frequency identified by Bo *et al.* (2012) even at the symmetry plane. The authors also confirmed the results of Adler & Gaitonde (2018) that, for the uncontrolled SBLI, the recirculation bubble is modulated by a mode at a Strouhal number based on the separation length $St_{L_{sep}} = 0.1$, an order of magnitude larger than that of the shock unsteadiness. For the controlled case, instead, the recirculation bubble is synchronised with the shock motion at a Strouhal number of approximately $St_{L_{sep}} = 0.05$. However, no physical explanation was provided regarding the mechanism behind this synchronisation.

The above literature review indicates that relevant research questions about the control of SBLI through MVGs remain open. The interpretation and description of the mean and instantaneous wake from the microramp is still debated. The effects of the three-dimensional (3-D) and unsteady changes in the separation topology are unclear. Regarding the low-frequency unsteadiness, there is no clear physical explanation of the observed increase in the distinctive low frequency in the controlled case, and further analysis is necessary to characterise and understand the effects of the periodic disruption of the reflected shock surface associated with the passage of the arch-like vortices. In addition, despite being known that the shock unsteadiness is strongly intermittent (Dolling 2001), little is known regarding if and how microramps affect this intermittency. Bernardini *et al.* (2023*a*) showed through wavelet analysis that the broadband shock motion can be interpreted as the result of a collection of sparse events in time, each characterised by its temporal scale. How these events are affected by the unsteady and 3-D changes in SBLI due to MVGs is yet to be discussed.

From a methodological point of view, DNS data are relatively scarce and limited to compression-ramp SBLIs in hypersonic flow conditions only (Sun *et al.* 2019, 2020), despite the complex 3-D and unsteady nature of the flow may benefit from a description without simplifying and modelling assumptions. Indeed, several studies (Ghosh *et al.* 2008) proved that Reynolds-averaged Navier–Stokes simulation (RANS) methodology with traditional eddy-viscosity turbulence models is completely inadequate even to predict only the mean field, but also that ILES methods fail to accurately reproduce experimental data (Lee *et al.* 2010), which, in turn, suffer from known limitations in resolution and data accessibility. Moreover, high-fidelity data from DNSs may be extremely useful, as they provide a precious reference to assess the results of low- and mid-fidelity numerical simulations, and they may even serve as input for data-driven reduced order models with a dramatically reduced computational cost.

Given this scenario, this work examines the DNS database of a SBLI generated by an oblique shock wave impinging on a turbulent boundary layer in the presence of an infinite array of microramp MVGs, to investigate how microramps alter the flow physics of a traditional 2-D SBLI. Indeed, we point out that, rather than focusing on the specific study of the MVGs control effectiveness or on the possible strategies to improve their current design, this study primarily aims at characterising the flow physics associated with microramp-controlled SBLIs. The turbulent boundary layer considered has a free-stream Mach number $M_\infty = U_\infty/a_\infty = 2.28$ and a friction Reynolds number at the shock impingement location $Re_\tau = \rho_w \delta u_\tau/\mu_w \approx 600$, where U_∞ is the free-stream velocity, a_∞ is the free-stream speed of sound, ρ_w is the density at the wall, δ is the boundary layer thickness, $u_\tau = \sqrt{\tau_w/\rho_w}$ is the friction velocity, τ_w is the wall shear stress and μ_w is the dynamic viscosity at the wall. The shock generator has an angle $\alpha = 9.5°$, while the microramp geometry and position are based on the optimal set-up indicated by Anderson *et al.* (2006).

The analysis compares the results of two simulations, the uncontrolled SBLI, indicated in the following as USBLI, and the controlled SBLI, indicated in the following as CSBLI. The qualitative and quantitative effects of the microramps on SBLI are assessed in terms of both the mean and the instantaneous flow field, while trying to provide physical explanations for some of the open issues that we highlighted. Moreover, the long integration period covered by the simulations makes it possible to consider the effects of microramps on the SBLI low-frequency unsteadiness, which is studied using both traditional Fourier spectra and wavelet analysis in the time/frequency domain.

The paper is organised as follows: § 2 presents the methodology and numerical set-up of the simulations; § 3 describes the database generated and the validation carried out; § 4 presents the analysis of the results; finally, § 5 reports some final comments.

2. Methodology and numerical set-up

DNSs have been carried out using STREAmS 2.0 (see https://github.com/STREAmS-CFD/STREAmS-2) (Bernardini *et al.* 2021, 2023*b*; Sathyanarayana *et al.* 2023). STREAmS is an open-source, finite-difference flow solver designed to solve the compressible Navier–Stokes equations for a perfect, heat-conducting gas in canonical wall-bounded turbulent high-speed flows. The solver is oriented to modern CPU-GPU high-performance computing (HPC) platforms and has been validated extensively in recent works (Della Posta *et al.* 2023*b*; Yu, Modesti & Pirozzoli 2023).

The convective terms are discretised through a hybrid energy-conservative/shock-capturing approach in a locally conservative form. In smooth regions, stability is maintained using a sixth-order, central, energy-preserving flux formulation, avoiding
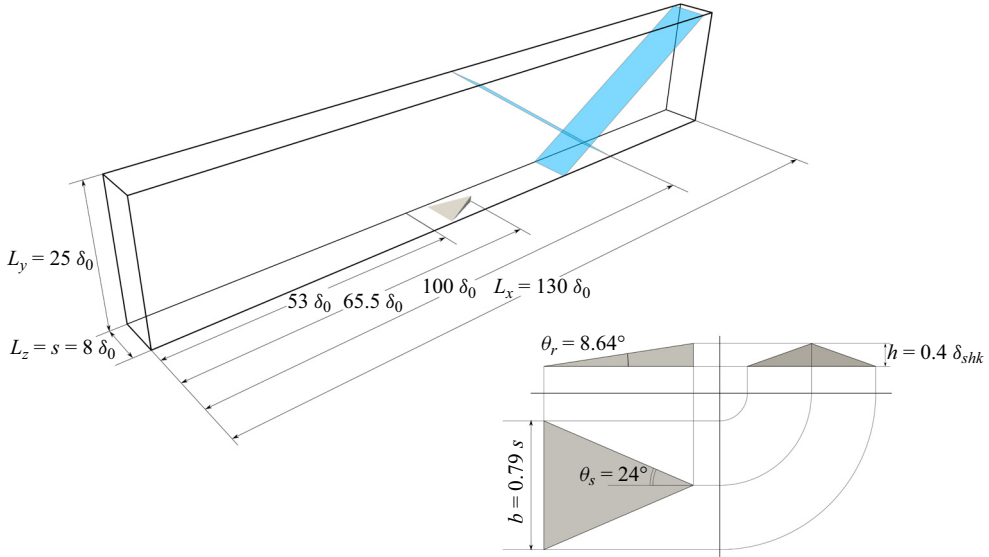
Figure 1. Domain with sizes and orthogonal projections of the microramp.

the need for additional numerical diffusivity. Near shock waves, a fifth-order weighted essentially non-oscillatory (WENO) reconstruction (Jiang & Shu 1996) is applied to calculate numerical fluxes at cell faces, using a Lax–Friedrichs flux vector splitting. A modified version of the Ducros shock sensor (Ducros *et al.* 1999)

$$\theta = \max\left(-\left(\boldsymbol{\nabla} \cdot \boldsymbol{u}\right) / \sqrt{(\boldsymbol{\nabla} \cdot \boldsymbol{u})^2 + |\boldsymbol{\nabla} \times \boldsymbol{u}|^2 + u_0^2/L_0}, 0\right) \in [0, 1], \qquad (2.1)$$

where $\boldsymbol{u}$ is the instantaneous velocity, while u_0 and L_0 are suitable velocity and length scales, assesses the local smoothness of the solution, determining the presence of discontinuities where central and WENO schemes switch. Viscous terms are approximated using sixth-order, central finite-difference formulae. Time advancement is achieved through a third-order, low-storage Runge–Kutta scheme (Spalart, Moser & Rogers 1991).

The size of the computational domain adopted is $L_x/\delta_0 \times L_y/\delta_0 \times L_z/\delta_0 = 130 \times 25 \times 8$, with δ_0 being the thickness of the boundary layer at the inflow. The geometrical set-up of the microramp is based on the optimal configuration defined by Anderson *et al.* (2006) (see figure 1 and table 1), with a ratio between the ramp height and the boundary layer thickness at the inviscid shock impingement location equal to $h/\delta_{shk} = 0.40$ ($h/\delta_0 = 1.073$) and a distance from the ramp trailing edge and the inviscid shock impingement location equal to $14.16\delta_{shk}$. The microramp is centred in the spanwise direction ($z_{TE} = L_z/2$) and is simulated using a ghost-point-forcing immersed boundary method (IBM) (Piquet, Roussel & Hadjadj 2016) already validated in previous works (Della Posta *et al.* 2023b). Lateral periodic boundary conditions allow representing an infinite array of microramps with the Anderson's optimal lateral spacing $s/h = L_z/h = 7.46$ (corresponding to $L_z/\delta_{LE} \approx 3.85$, with δ_{LE} being the boundary layer thickness at the ramp leading edge) and a microramp width $b = 0.79\,s$, despite considering a single microramp only in the computational domain.

At the outflow and the top boundaries, non-reflecting conditions are imposed by performing a characteristic decomposition in the direction normal to the boundaries (Poinsot & Lele 1992). Inviscid shock relations are set at the top boundary to impose

998 A12-6

h/δ_{shk}	θ_s	θ_r	d/δ_{shk}	s/h
0.40	24°	8.64°	14.16	7.46

Table 1. Main geometrical parameters of the microramp based on the optimal configuration of Anderson *et al.* (2006) (see figure 1): *h* is the height of the microramp, δ_{shk} is the boundary layer thickness at the inviscid shock impingement, θ_s and θ_r are the wedge half-angle and the elevation angle of the ramp respectively, *d* is the distance between the microramp trailing edge and the streamwise position of the inviscid shock impingement and *s* is the spanwise spacing between two consecutive microramps.
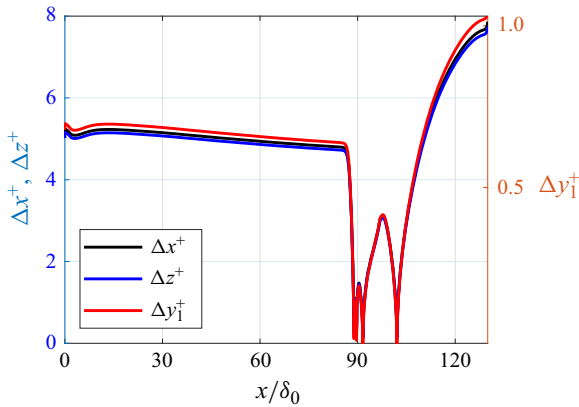
Figure 2. Grid spacing in local wall units along the streamwise direction for the USBLI case.

the presence of the shock generator, such that the inviscid shock impingement x_{imp} at the wall is at $100\delta_0$ from the inlet. A characteristic wave decomposition is also employed at the bottom no-slip wall, where the wall temperature is set to the recovery value of the incoming boundary layer to impose weak adiabatic wall conditions. A recycling–rescaling procedure (Lund, Wu & Squires 1998) is used to provide the inflow with suitable turbulent fluctuations. The recycling station is placed at $53\ \delta_0$ from the inflow to guarantee a sufficient decorrelation between the inlet and the recycling station.

The mesh is uniform in the wall-parallel directions, corresponding to a viscous-scaled wall spacing before the interaction of $\Delta x^+ = 4.79$ and $\Delta z^+ = 4.72$. A physics-driven grid distribution specifically designed by Ceci & Pirozzoli (2023) for the simulation of compressible turbulent wall-bounded flows is used instead in the wall-normal direction. The stretching function blends a uniform near-wall spacing with $\Delta y^+ \approx 1$ with a uniform outer layer resolution in terms of semi-local Kolmogorov units. Note that this choice allows having a fine grid also in the irrotational region outside the boundary layer, which is needed to have an appropriate resolution of the oblique shock waves. The resolution is such that, before the interaction, $\Delta y_1^+ = 0.64$ and $\Delta y_\delta^+ = 8.73$, with Δy_1 and Δy_δ being the wall-normal spacing at the wall and at the boundary layer edge, respectively. The wall grid spacing in local viscous units along the three coordinate directions is reported in figure 2 for the USBLI case. Moreover, we verified that the grid spacing $\Delta = (\Delta x\, \Delta y\, \Delta z)^{1/3}$ never exceeds $3.6\ \eta$, which is smaller than the typical size of the small-scale eddies ($5 \div 6\eta$ according to Jiménez & Wray (1998) and Pirozzoli, Bernardini & Grasso (2008)) and thus indicates that all the scales of the flow motion are adequately resolved even in the interaction region.

M_∞	α	Re_τ	Re_θ	Re_{δ_2}	$N_x \times N_y \times N_z$	$\dfrac{T\,U_\infty}{L^u_{sep}}$
2.28	9.5°	505 (TE)	2584 (TE)	1560 (TE)	$6144 \times 512 \times 384$	3108 (USBLI)
		599 (shk)	3205 (shk)	1935 (shk)		1595 (CSBLI)

Table 2. Main flow parameters of the numerical database. Here Δt is the sampling time step used to record unsteady data and T is the total time considered for statistics. TE, property at the microramp trailing edge; shk, property at the inviscid shock impingement; USBLI, uncontrolled SBLI; CSBLI, microramp-controlled SBLI.

Unless specified, the coordinates are expressed in terms of the separation length of the uncontrolled case L^u_{sep}, according to which $x^* = (x - x_{imp})/L^u_{sep}$, $y^* = y/L^u_{sep}$ and $(z - z_{TE})/L^u_{sep}$. A total time of 3108 L^u_{sep}/U_∞ for the USBLI case and of 1595 L^u_{sep}/U_∞ for the CSBLI case has been recorded, with L^u_{sep} being the separation length of the uncontrolled case. Considering that the non-dimensional characteristic low frequency typically stands in the range $St = f\,L^u_{sep}/U_\infty \in [0.02, 0.06]$, the period considered corresponds to 60–190 and 30–100 cycles for the USBLI and CSBLI cases, respectively. The non-dimensional sampling frequency recorded is equal to $L^u_{sep}/(U_\infty \Delta t) = 2.0139$.

3. Numerical data set and validation

The main parameters of the numerical database analysed in this work are reported in table 2. The data set includes a baseline simulation with the undisturbed SBLI, which is used as a reference to assess the effects of the microramps, and the same SBLI controlled by the microramp. The friction Reynolds number of the incoming boundary layer based on the properties at the shock impingement location is approximately 600, corresponding to momentum-based Reynolds numbers $Re_{\delta_2} = \rho_\infty U_\infty \theta/\mu_w$ equal to 1935 and $Re_\theta = \rho_\infty U_\infty \theta/\mu_\infty$ equal to 3205. The free-stream Mach number M_∞ is equal to 2.28, while the shock generator has an angle of 9.5°.

3.1. *Boundary layer validation*

To validate the state of the incoming turbulent boundary layer impinging on the microramp, figure 3 shows the wall-normal distribution of the van Driest-transformed mean velocity profiles and of the density-scaled Reynolds stress components. Results from a section at the ramp trailing edge of the USBLI case ($Re_\tau \approx 505$) are compared with the reference DNS data from Pirozzoli & Bernardini (2011) ($M_\infty = 2.0$, $Re_\tau = 580$) and from Jiménez *et al.* (2010) (incompressible, $Re_\tau = 580$). A satisfactory agreement can be observed for the mean velocity from the viscous sublayer up to the outer region with both references. The density-scaled Reynolds stress components are instead reported in figure 3(*b*), showing again results close to the reference data, with only slight and tolerable departures, considering the different flow conditions of the cases reported.

3.2. *Microramp wake validation*

To validate the development of the wake behind the microramp, figure 4 reports two wake properties along the streamwise direction typically considered for microramps and which have been demonstrated to be rather independent of the flow conditions in terms of Mach and Reynolds numbers. In particular, figure 4(*a*) reports the streamwise evolution
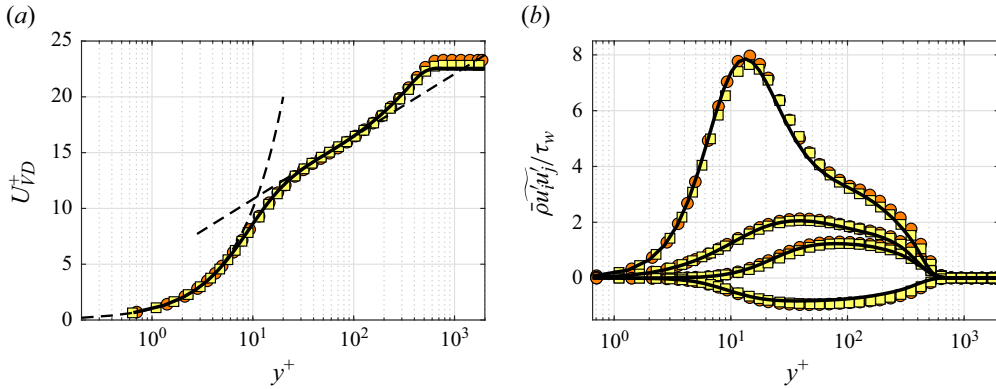
Figure 3. Comparison of (*a*) van Driest–transformed mean velocity profile and (*b*) density-scaled Reynolds stress components for the incoming boundary layer (solid black line, USBLI data at streamwise position of the ramp trailing edge, $Re_\tau \approx 505$) with other DNS reference data by Pirozzoli & Bernardini (2011) (orange circles, $M_\infty = 2$, $Re_\tau = 580$) and Jiménez *et al.* (2010) (yellow squares, incompressible, $Re_\tau = 580$).

Case	a_u	b_u	a_v	b_v
Grébert *et al.* (2023)	1.60	−0.64	4.00	−1.41
Present data	1.31	−0.59	2.72	−1.27

Table 3. Coefficients defining the fitting $a(x/h)^b$ for the wake and upwash velocities distributions along the streamwise coordinate.

of the Favre-averaged wake velocity $\tilde{u}_{wake}/U_\infty$, which is defined as the velocity in correspondence with the minimum difference between the controlled and the uncontrolled velocity profiles at the symmetry plane. The wake velocity represents a measure of the intensity of the low-momentum region generated by the microramp and progressively increases proceeding downstream as the wake decays by the action of molecular and turbulent mixing. Present results are compared with the experimental measurements of Giepman *et al.* (2015) for two values of the relative height of the microramp similar to the case under study and with the empirical fitting proposed by Grébert *et al.* (2023) of the form $a\,(x/h)^b$. The fitting was based on LES data and describes the far wake evolution of a similar configuration having, however, higher Mach and Reynolds numbers ($M_\infty = 2.7$ and $Re_\theta = 3600$, based on the momentum thickness $1.5\,L_{sep}$ upstream of the inviscid impingement). The data agree well with the results from the literature in the far wake, and the rates resulting from power-law fittings considering only results from $x/h \geq 10$ comply fairly with those estimated by Grébert *et al.* (2023). Table 3 reports a comparison of the coefficients from least-square data fitting. Figure 4(*b*) shows instead a similar comparison for the peak Favre-averaged lift-up velocity $\tilde{v}_{max}/U_\infty$, which is the maximum value of the vertical velocity component along the wall-normal coordinate at the symmetry plane. The peak lift-up velocity represents a measure of the intensity of the lift-up mutually induced by the primary vortex pair at the symmetry plane, which gradually pushes the wake farther from the wall. As for the wake velocity, the agreement with the literature results is satisfactory, with discrepancies mainly related to the different Reynolds and Mach numbers between simulations and experiments, as shown in Della Posta *et al.* (2023) and Della Posta *et al.* (2023*a*).
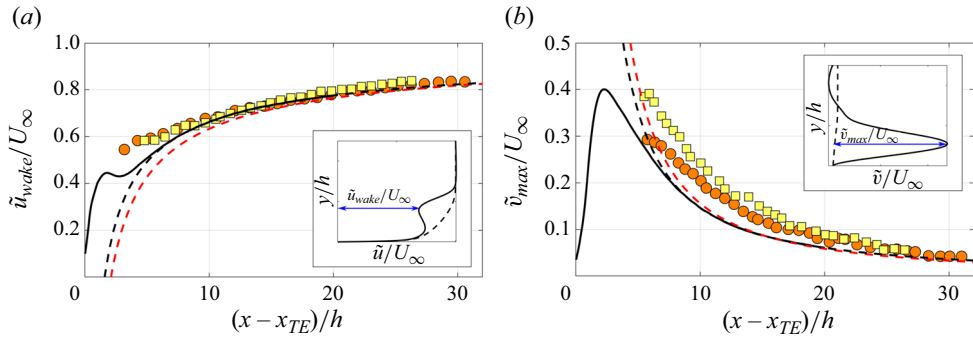
Figure 4. Streamwise evolution of (*a*) wake velocity and (*b*) upwash velocity at the symmetry plane. Experimental data from Giepman *et al.* (2016) (orange circles $h/\delta = 0.35$, yellow squares $h/\delta = 0.46$), present data (solid black line), data fitting of LES results from Grébert *et al.* (2023) (dashed red line), data fitting of present data (dashed black line). Small insets illustrate the definition of the two velocities from the velocity profiles of the controlled (solid) and uncontrolled (dashed) cases.

4. Results

4.1. *Qualitative flow organisation*

To first understand the qualitative flow organisation, figure 5 reports an instantaneous visualisation of the turbulent and shock structures in the flow field using an isosurface of the swirling strength coloured by the streamwise velocity and an isosurface of the shock sensor θ. A video of the flow, generated using *in situ* visualisation at runtime (Bnà *et al.* 2023), is linked in the supplementary material. In addition to the shocks associated with the uncontrolled SBLI, another shock system is visible in correspondence with the microramp, which has been characterised extensively in previous works (Della Posta *et al.* 2023). In particular, an almost-planar shock wave is generated at the leading edge of the ramp, while a conical shock wave surrounds the wake from the trailing edge. These weak shocks interact with the main impinging shock far from the wall. The turbulent structures show, instead, how the incoming flow is first captured at the sides of the microramp, thus generating the primary vortex pair and then the arch-like vortices around the ramp wake. However, the most notable differences with the traditional uncontrolled SBLI take place in correspondence with the foot of the reflected shock wave, whose shape is altered significantly by the incoming flow. The lower part of the shock is completely disrupted at the centre of the domain, where the ramp wake hits the interaction, and bulges are periodically generated when the K–H vortices around the wake pass through the shock. The spanwise alteration of the separation region, which is, however, still present as it can be observed from the presence of reversed flow between the shocks, also affects the flow downstream of the interaction region, where the compression wave after the separation is no longer homogeneous in the spanwise direction.

The differences along the span of the microramp-controlled SBLI are also visible in the instantaneous temperature contours at the symmetry and lateral *xy* planes (figure 6). While the lateral slice reminds of a traditional 2-D SBLI, only with the addition of two extra shocks upstream, the billows of the ramp wake completely alter the incoming flow (as observed in Bo *et al.* 2012), the interaction region and the downstream flow at the symmetry plane, with a significantly thicker boundary layer.

As anticipated, the presence of the MVG radically affects the incoming boundary layer, which shapes the interaction region in turn. Typical near-wall streaks, observable in the velocity contours on *xz* planes in figure 7, are now overlapped to the large-scale trace of the
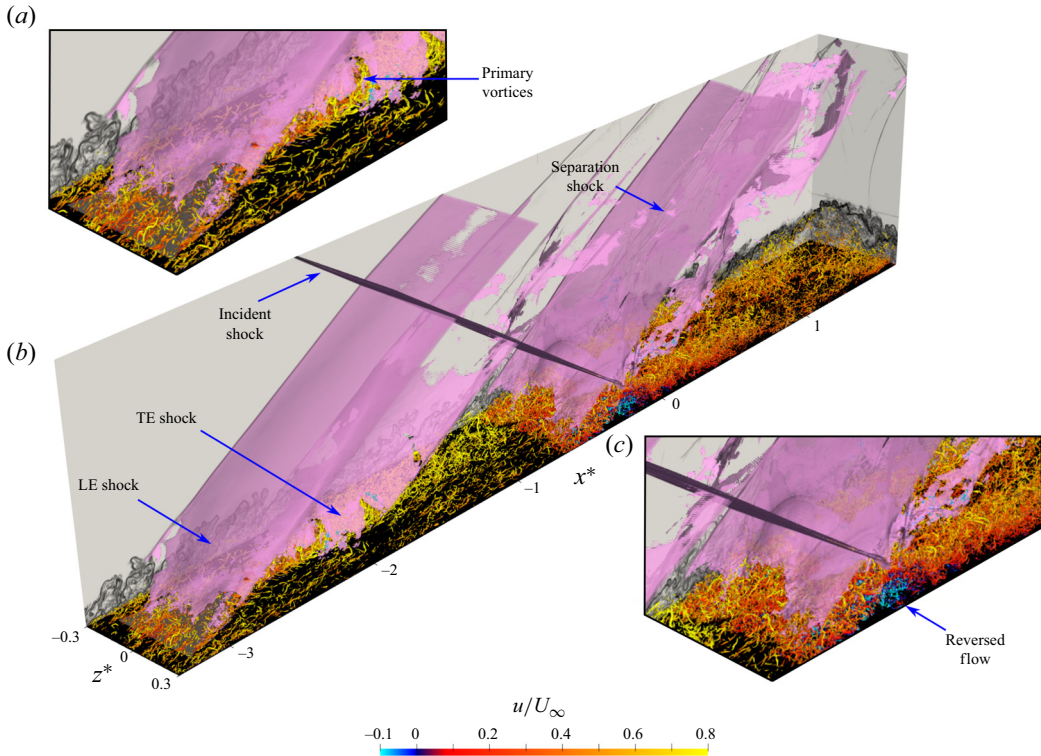
Figure 5. Instantaneous visualisation of the turbulent and shock structures. Isosurface of the swirling strength coloured by the streamwise velocity component ($\lambda_{ci}L^u_{sep}/U_\infty = 60$), isosurface of the shock sensor in pink ($\theta = 0.9$), numerical schlieren on the xy and yz slices in the background. Insets show a enlarged view of the microramp (*a*) and interaction (*c*) regions.

ramp wake. On the one hand, the low-momentum wake decelerates the flow at the centre of the domain, corresponding to an increase in the reversed flow extent. On the other hand, the vortical motion of the primary vortices and the transversal mixing associated with the arch-like vortices promote local accelerations of the flow, corresponding to a decrease in the reversed flow. Before and even after the interaction, the meandering motion of the ramp wake and the spanwise alteration of the separation generate the formation of alternated regions of accelerated and decelerated flows, similar to large-scale streak structures.

4.2. *A 2-D view: a classic 2-D SBLI analysis*

Although the qualitative flow description confirmed the literature findings about the increased geometrical complexity of the 3-D flow field for the controlled SBLI, figure 8 shows that the streamwise distribution of the wall-pressure rise is homogeneous in the span, as also observed in the experimental measurements of Babinsky *et al.* (2009), although tiny differences across the span are visible in the interaction region where the streamwise pressure gradient is minimum. The figure reports the wall pressure at three notable sections in the span, which are: the symmetry plane $z^* = 0$, the lateral plane $z^* \approx -0.30$ and the spanwise section corresponding to the minimum streamwise extent of the separation, $z^* = -0.0513$ (see § 4.3). The curves show that, compared with the USBLI case, the presence of the microramp induces a downstream shift in the separation onset
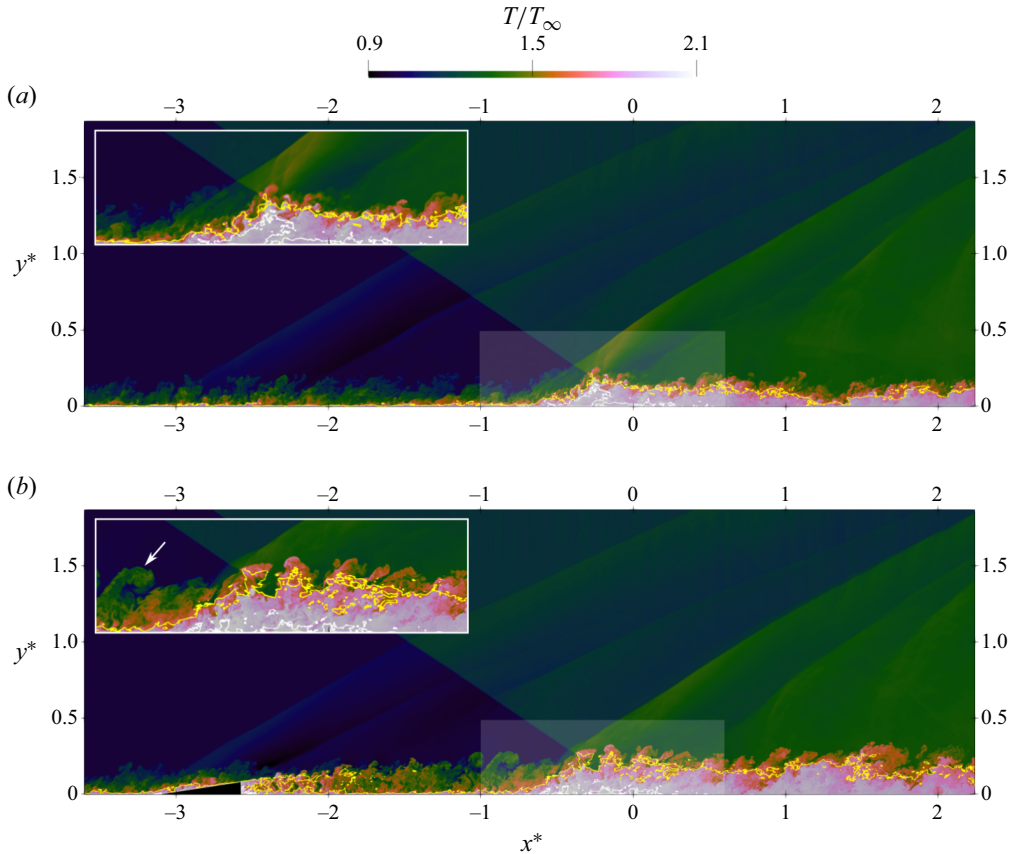
Figure 6. Instantaneous temperature on xy planes at (*a*) $z^* = -0.3$ and (*b*) $z^* = 0.0$. The white lines indicate $u/U_\infty = 0$, while the yellow lines indicate points with $M = 1$. Enlarged views of the separation region are shown in the insets. An arrow indicates a sample billow in the microramp wake.

(indicated with circles) and a slight upstream shift in the reattachment (indicated with squares), which thus entails an overall shorter separation along the span. The wall-pressure standard deviation σ_{p_w} at the same sections shows instead that wall-pressure fluctuations are stronger for CSBLI. As in the case of non-adiabatic wall conditions (Bernardini *et al.* 2016) or transitional SBLIs (Quadros & Bernardini 2018), a reduction (increase) of the separation length corresponds to an increase (decrease) in the intensity of the wall-pressure fluctuations. The CSBLI curves also present another peak in the rear part of the separation and, most importantly, vary considerably with the span (see § 4.3). In particular, the standard deviation distribution in the interaction region is minimum at the symmetry plane and maximum at the lateral plane, despite having similar values upstream of the separation onset. Indeed, as the increase in σ_{p_w} induced by the microramp wake decays quite fast (faster at the symmetry plane) before the interaction region, it is reasonable to believe that the different behaviour for the three sections is more related to spanwise modifications of the shock surface and the separation bubble, or even to 3-D effects, rather than to the vanishing effect of the microramp wake itself (see § 4.3). After the separation, the decay rate of σ_{p_w}/p_∞ is larger in CSBLI than in USBLI, and rather homogeneous in the span.

Figure 9 reports instead the distribution of the time-averaged streamwise skin friction component $\overline{C_{f,x}}$ at different sections in the span. As shown by the spanwise-averaged curve
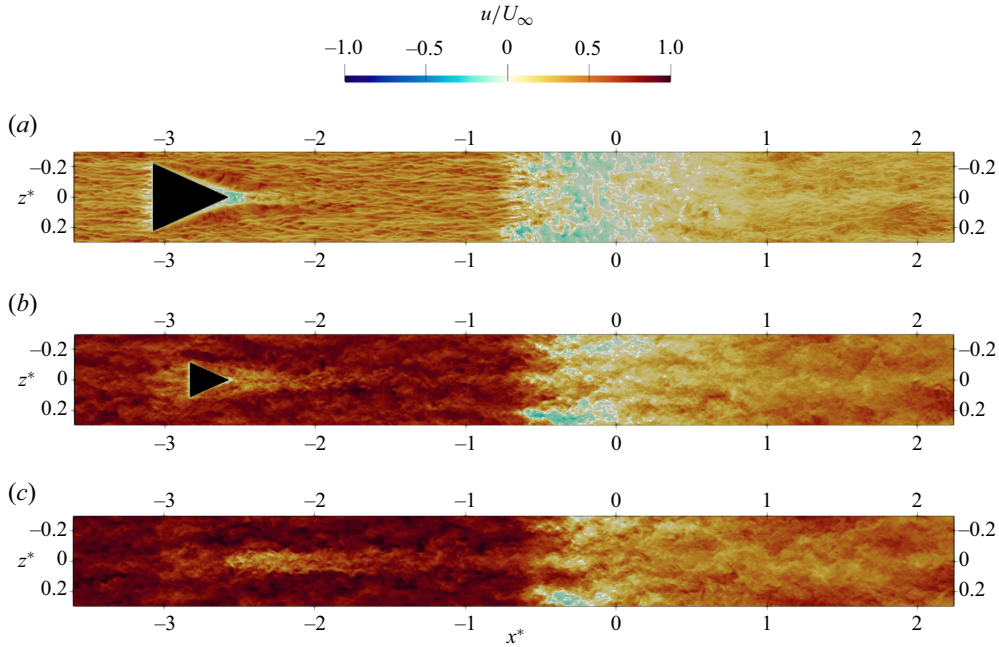
998 A12-12

Figure 7. Instantaneous streamwise velocity on xz planes at (a) $y^+ = 1$, (b) $y/h = 0.5$ and (c) $y/h = 1$. The white lines indicate $u/U_\infty = 0$.
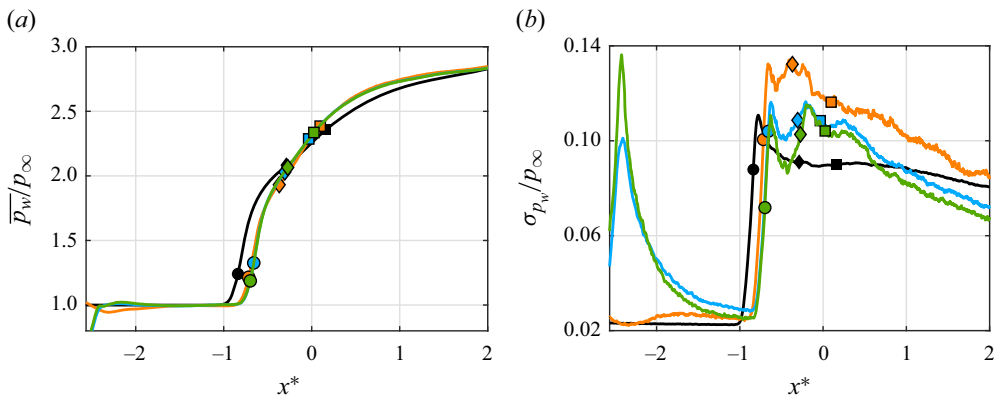

Figure 8. Streamwise distribution of (a) mean wall pressure and (b) wall-pressure standard deviation. Spanwise average of the uncontrolled case (solid black line), controlled case at $z^* = -0.2986$ (solid orange line), $z^* = -0.0513$ (solid light blue line) and $z^* = 0.0$ (solid green line). Symbols indicate the location of the separation point (circles), the reattachment point (squares), and the point with minimum streamwise pressure gradient (diamonds) for the curve of the corresponding colour.

of the CSBLI case, the extent of the region with negative $\overline{C_{f,x}}$ is shortened significantly compared with the USBLI case. However, we also note in this case that conditions vary considerably with the span when the microramp is present, suggesting that the streamwise skin friction component alone may provide misrepresentative information regarding the extent and the nature of the separation, because of the non-negligible contribution of the spanwise skin friction component.
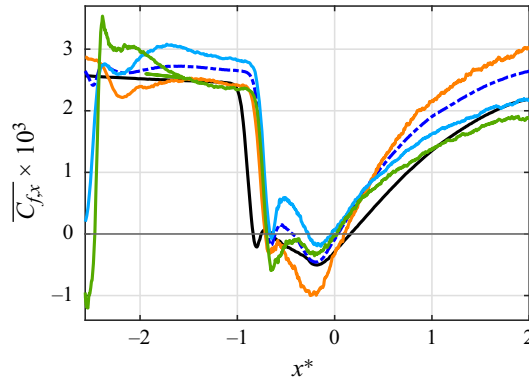
Figure 9. Streamwise distribution of the streamwise skin friction coefficient. Spanwise average of the uncontrolled case (solid black line), spanwise average of the controlled case (dashed-dotted blue line), controlled case at $z^* = -0.2986$ (solid orange line), $z^* = -0.0513$ (solid light blue line) and $z^* = 0.0$ (solid green line).

The significant spanwise modulation of the flow is also observed in the *xy*-slices of figure 10, which compares the Favre-averaged streamwise velocity component for the USBLI case (spanwise-averaged) and for the three above-defined spanwise sections of the CSBLI case. To consider compressibility, Favre averages are used, which are defined as $\tilde{\phi} = \overline{\rho\phi}/\bar{\rho}$ for a generic variable ϕ. The reversed flow region is highlighted and hints that for the two inner sections, the separation is reduced relevantly. However, it is important to note that especially for strongly 3-D flow, as in the case under consideration, the reversed flow is not indicative of the actual separation taking place.

In conclusion, the wall-pressure standard deviation, the streamwise skin friction component, and the *xy* slices of the mean velocity proved that for many features, but not all, the flow organisation is fully 3-D, especially close to the wall and in the interaction region. The analysis of single streamwise slices of the streamwise components of vectorial quantities may thus be insufficient or even misleading in trying to understand the overall interaction topology and dynamics.

4.3. *More than 2-D: the controlled SBLI separation*

Given the three-dimensionality of the separation, we must resort to more sophisticated tools for its analysis. Following the work of Legendre & Werlé (Délery 2001; Délery 2013), the topology of the separation can be examined by studying the organisation of the skin friction lines at the wall. Skin friction lines can be viewed as the limit towards the wall of the streamlines and, if a mean flow is well-defined, they can provide insightful information about the actual location of the separation and reattachment.

Figure 11 reports the skin friction lines for the CSBLI case on half of the domain, taking advantage of the flow case symmetry (see Appendix A for a discussion on this assumption), and highlights the formation of curved separation and reattachment lines along the span, where skin friction lines converge to and depart from, respectively. Critical points ($C_{f,x} = C_{f,z} = 0$) are also highlighted according to their nature: saddle points indicated as light green circles, nodes as light blue squares, and foci as orange diamonds. For the sake of completeness, we remind the reader that only two skin friction lines run through a saddle point, while all the others avoid it adopting the shape of a hyperbolic curve, that all the skin friction lines have a common tangent at a node, except for one of
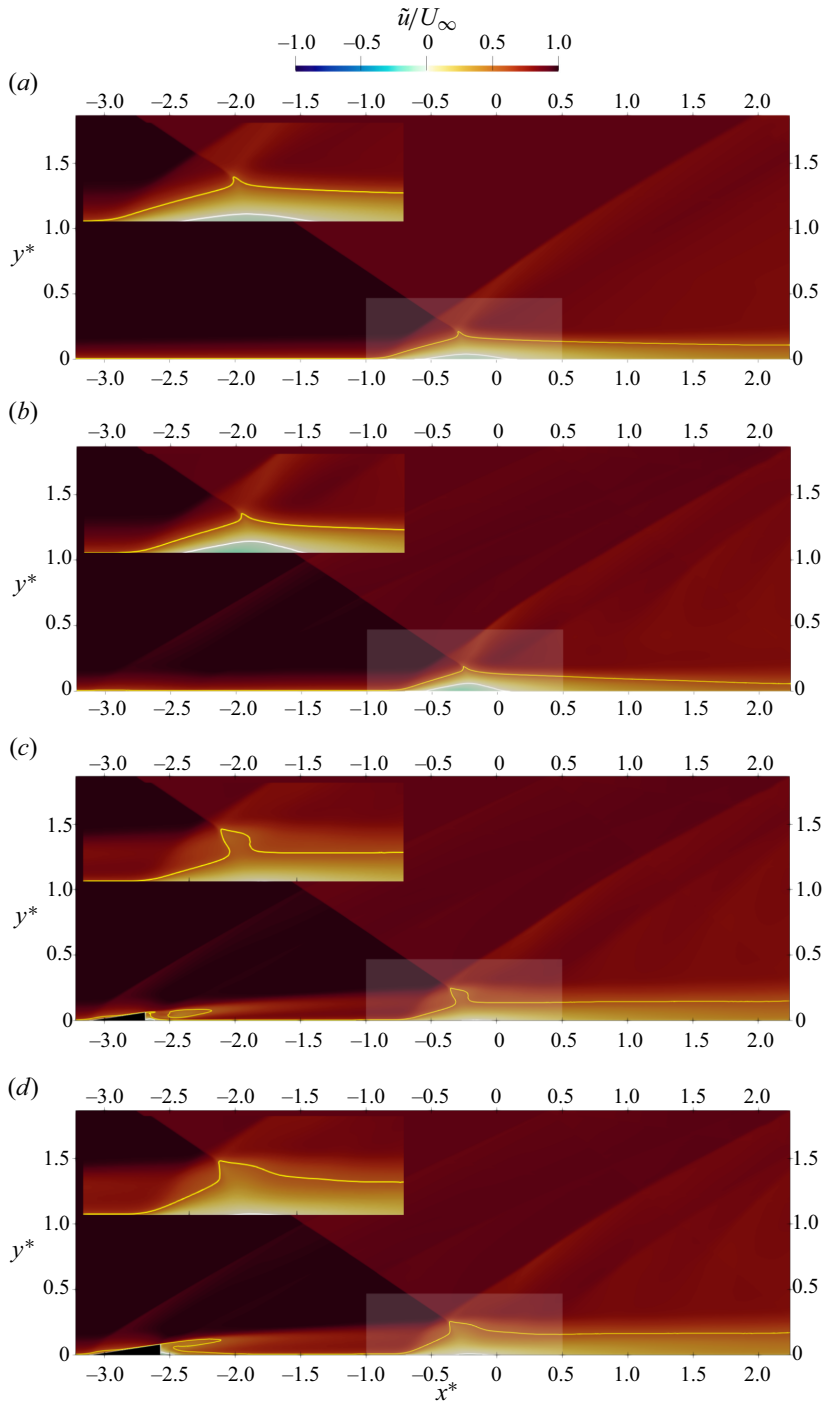
Figure 10. Favre-averaged streamwise velocity on xy planes: (*a*) USBLI, spanwise-averaged, and CSBLI at (*b*) $z^* \approx -0.3$, (*c*) $z^* = -0.05$ and (*d*) $z^* = 0$. Yellow lines indicate points with $\widetilde{M_\infty} = 1$, white lines indicate points with $\tilde{u}/U_\infty = 0$. Enlarged views of interaction regions are given at the top left corner of each subfigure.

them, and that skin friction lines end at a focus after spiralling around it. Considering also the symmetric half not shown in the figure, the periodic boundary conditions, and the two nodes at infinite upstream and downstream, our configuration for the interaction region (figure 11c) has a total of five nodes ($n = 5$), four foci ($f = 4$) and seven saddle points ($s = 7$), which satisfies the necessary topological condition $n + f - s = 2$ (Délery 2013). Our arrangement has one node, two foci and three saddle points more than that in Grébert *et al.* (2023), as the separation line is split into more than one single segment in our case. As a result, the scenario describes a more complex arrangement of the trailing vortices after reattachment, which suggests a difference in intensity, height and development of the primary vortices after the interaction, likely due to the different flow conditions of the incoming flow considered. Moreover, it is possible to see that close to the symmetry plane, the organisation of the main reattachment line is not as clear as in the rest of the plane. The elusive location and nature of the critical points suggest that, despite the long integration period considered, the mean skin friction lines may have not reached here a proper steady-state representative of the flow behaviour above the wall, which thus asks for further research.

The focus, already observed also in oil-flow visualisations (Babinsky *et al.* 2009), indicates the presence of a tornado-like structure which captures the flow close to the wall and pushes it upwards. A visualisation of the streamlines associated with the tornado in figure 12(b) shows that this structure tilts outwards to join the wall region closer to the symmetry plane and the external sides of the separation bubble. Indeed, its axis is first normal to the wall in correspondence with the focus and ends up being aligned with the spanwise direction towards the side.

Compared with the classical 2-D recirculation bubble, the region of separated flow is now more complicated and not identified by the simple condition of negative $\overline{C_{f,x}}$. Moreover, reversed flow is now even less indicative of the separation, which makes it difficult to identify the edge of the recirculating bubble. Figure 12(a) uses streamlines to show the qualitative shape of the bubble, which presents a characteristic saddle shape with a higher separated region at the symmetry and the lateral planes and a lower separation region in correspondence with the minimal streamwise separation extent (see figure 14). The trace of the tornado is also visible in the mean wall pressure at the interaction region in figure 13, where the minimum associated with the vortex core is superposed to the stronger pressure rise induced by the separation shock, resulting in the mild irregularity in the span previously observed in figure 8.

Significant 3-D effects are also visible in the distribution of the wall-pressure standard deviation $\sigma_{p,w}/p_\infty$ in figure 11. Close to the microramp, we can notice regions with relevant pressure fluctuations associated with (i) the impingement of the flow of the primary vortices at the sides of the ramp towards the wall and (ii) the reattachment of the flow after the trailing edge and the following formation of the parallel, primary vortex pair. In the interaction region instead, we observe a first, stronger peak after the separation onset, whose streamwise position follows the separation front and whose magnitude is greater close to the lateral boundaries. The distribution is compatible with the observation that the shock is disrupted at the centre of the domain and, hence, weaker on average (the pressure jump induced by the separation shock at the symmetry plane is 13 % weaker than that at the periodic boundary). As a result of the reduced shock intensity, the amplification of the pressure fluctuations induced by the shock wave is weaker in the central region of the domain. A second peak, with a spanwise-modulated amplitude as well, takes place at approximately half of the separation, in correspondence with the peak height of the
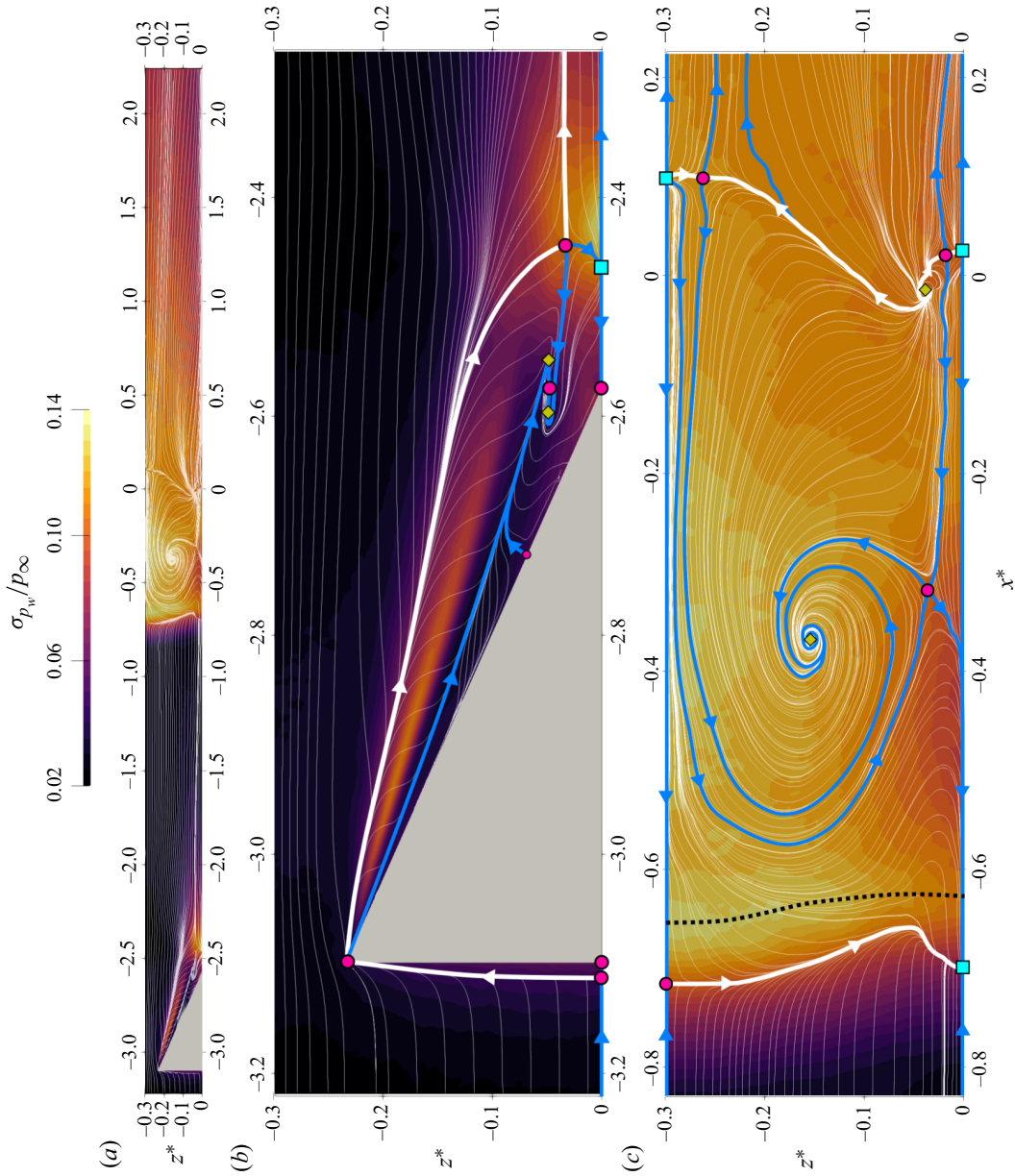
Figure 11. Skin friction lines overlapped to a contour of the wall-pressure standard deviation on the xz plane for the CSBLI case: (a) overall domain, (b) enlarged view of the ramp region and (c) enlarged view of the separation region. Half of the domain is shown for symmetry. Saddle points are indicated with circles in magenta, nodes with squares in light blue and foci with diamonds in orange. The main separation and reattachment lines are highlighted in white, other relevant critical lines in blue, whereas the foremost peak of σ_{p_w} is indicated with the dashed black line.
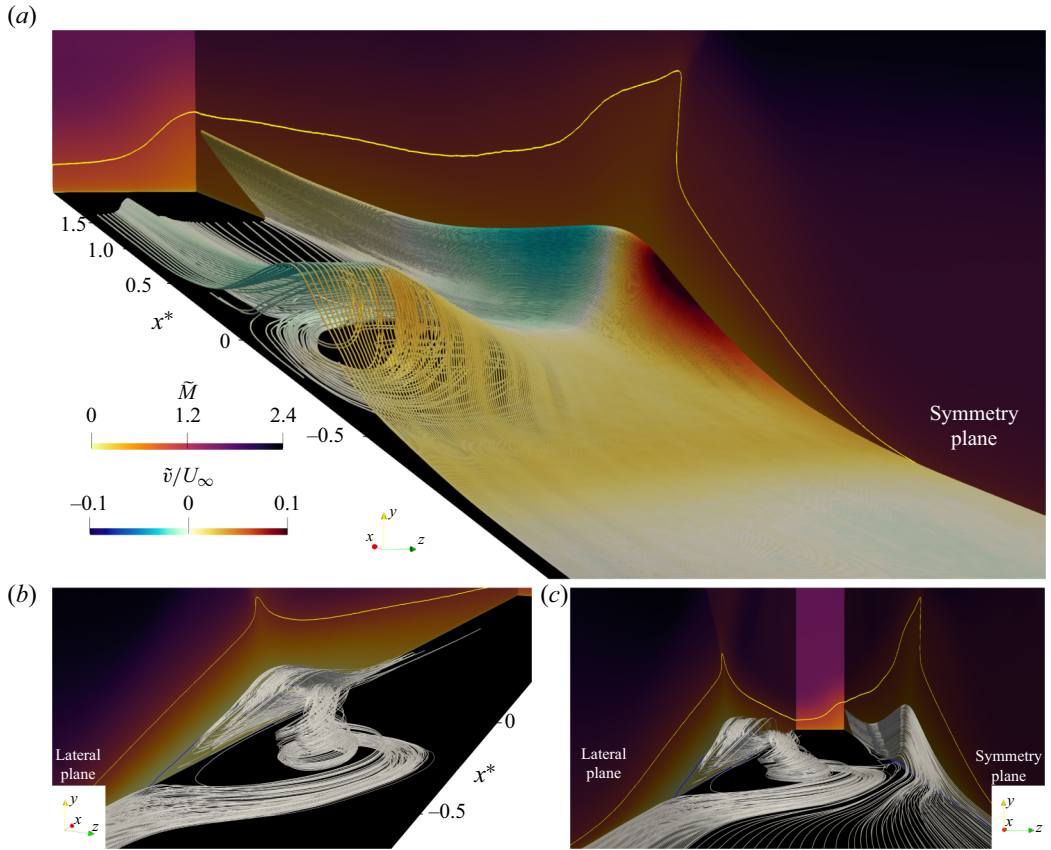
(*a*)

(*b*)

(*c*)

Figure 12. Streamlines in the separation region of the CSBLI case: (*a*) qualitative edge of the recirculation bubble (streamlines coloured by mean vertical velocity), (*b*) the tornado-like structure and (*c*) the internal structure of the bubble. Vertical slices report the Favre-averaged Mach number $\tilde{M}$, yellow lines indicate $\tilde{M} = 1$ and blue lines indicate $\tilde{u}/U_\infty = 0$ on the vertical slices at the symmetry and lateral planes. Half of the domain is shown for symmetry.
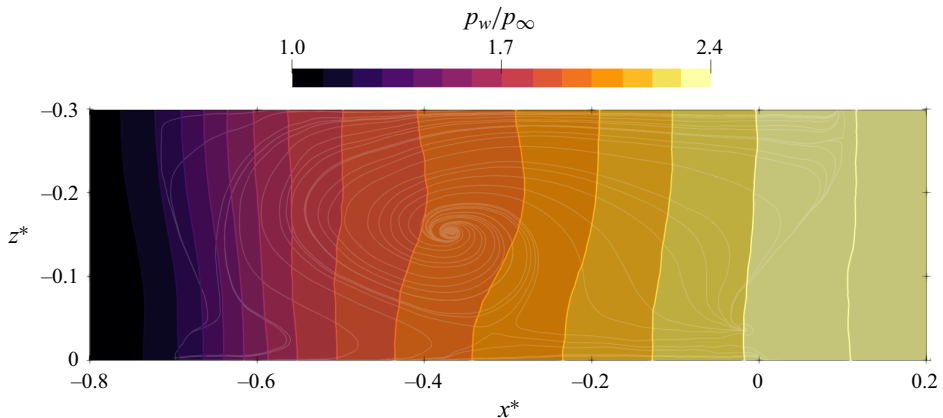

Figure 13. Wall pressure in the interaction region. Skin friction lines in the separation region are indicated in white. Half of the domain is shown for symmetry.
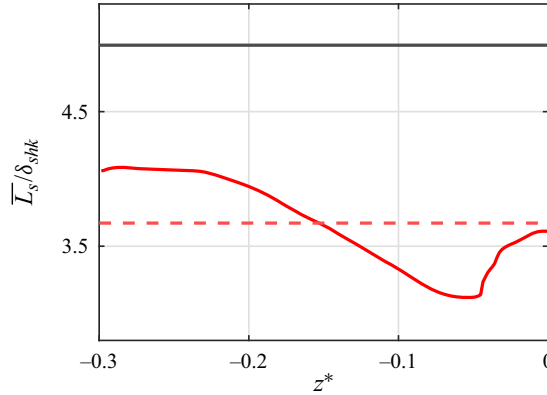
Figure 14. Spanwise distribution of the time-averaged separation length with respect to the boundary layer thickness at the shock impingement location. Spanwise average of the uncontrolled case (solid black line), local controlled case (solid red line) and spanwise average of the controlled case (dashed red line).

bubble. After the second peak, the standard deviation decays, maintaining a non-uniform spanwise distribution even far from the interaction.

Given the separation and reattachment line in figure 11, it is possible to estimate the extent of the time-averaged streamwise separation $\overline{L_s}$ along the span reported in figure 14. The spanwise average $\langle \overline{L_s} \rangle / \delta_{shk}$ shows that the mean separation in the presence of the microramp shrinks by 26.47 % the value observed in the USBLI case. Moreover, the distribution shows that the separation is largely modulated in the span, $(\overline{L_{smax}} - \overline{L_{smin}})/\langle \overline{L_s} \rangle = 26.31$ % along the span, with a minimal separation at $z^* \approx -0.05$ ($\overline{L_{smin}}/\delta_{shk} = 3.12$),

To understand the relationship between the spanwise modulation of the separation and the addition of momentum by the primary vortex pair, figure 15 reports the distribution of the compressible added momentum in the xz plane. First defined in its incompressible version by Giepman *et al.* (2014), the compressible added momentum is defined as

$$E_{add} = \int_0^{\overline{y^*}} \frac{\overline{\rho u^2}_{CSBLI} - \overline{\rho u^2}_{USBLI}}{\rho_\infty U_\infty^2} \, \mathrm{d}y \tag{4.1}$$

and tracks the addition of streamwise momentum towards the wall. Following Giepman *et al.* (2014), the upper bound of integration $\overline{y^*}$ is taken equal to $0.43\,\delta$, as the separation bubble was shown to be mostly sensitive to the momentum flux at y lower than this threshold. The distribution of E_{add}/h along the entire wall-parallel plane allows us to appreciate that the primary vortex pair brings fresh momentum towards the wall in a large spanwise range, even quite far from the symmetry plane. The peak added momentum just before the interaction is at $z^* \approx -0.1$, just at the side of the minimum separation, which thus suggests that the onset of the separation, and its local extent, follows strictly the addition of momentum associated with the primary vortex pair helical motion.

After a transitory region following the interaction, we can observe that the trace of the primary streamwise vortices becomes once again more visible, indicating that these are able to withstand the shock waves and that their signature lasts for a long streamwise distance (figure 15*a*). Even far downstream of the separation, we thus have non-uniform conditions as highlighted by figure 16 reporting the spanwise distribution at $x^* = 2$ of the incompressible shape factors and the streamwise skin friction coefficient for the USBLI and CSBLI cases. The shape factor denotes a fuller and healthier boundary layer even
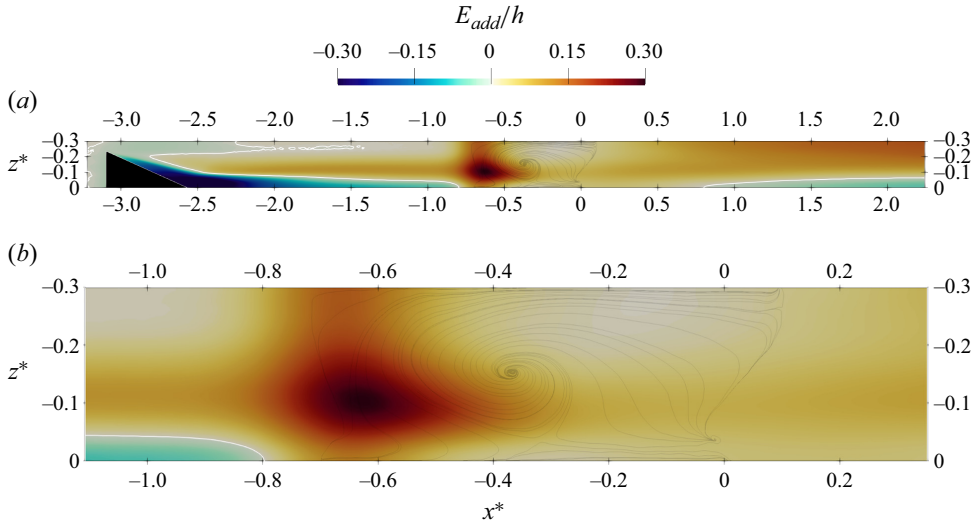
Figure 15. (*a*) Normalised compressible added momentum E_{add}/h along the xz plane and (*b*) enlarged view of the separation region. Skin friction lines in the separation region are indicated in grey. Half of the domain is shown for symmetry.
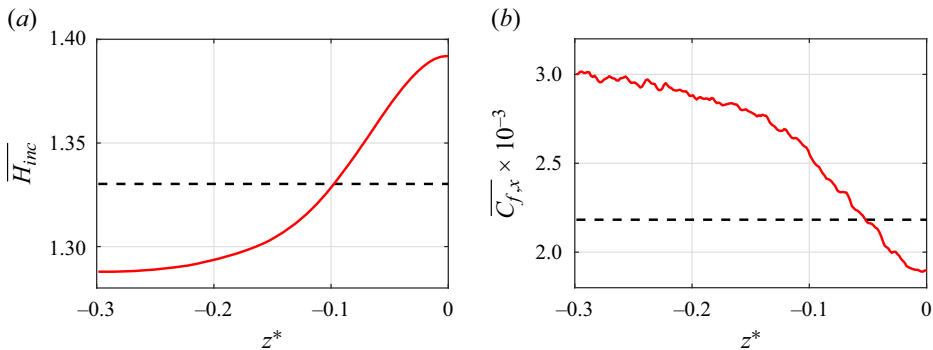

Figure 16. Spanwise distribution at $x^* = 2$ of (*a*) incompressible shape factor and (*b*) streamwise skin friction coefficient: USBLI (dashed black line) and CSBLI (solid red line).

after the interaction at the sides of the symmetry plane, which however corresponds to increased skin friction. We point out that the associated increased drag and the potential consequences of a long-lasting, non-uniform flow for the engine components following the inlet may limit the benefits of a reduced separation and thus that these aspects should be addressed carefully when considering MVGs for real applications.

Moreover, the fluid induces an additional drag force on the microramp itself that may be significant. We quantified this drag by defining an equivalent surface with the same overall drag of the ramp, with a width equal to s and a constant C_f equal to the skin friction at the leading edge of the ramp ($D = 1/2\rho_\infty U_\infty^2 C_{f,LE} L_x^D s$). The length of this surface L_x^D is equal to $2.52 L_{sep}^u$, meaning that, in terms of drag, the ramp is equivalent to a significantly longer boundary layer upstream of the interaction.

On the other hand, the momentum transfer towards the wall has a slight beneficial effect in terms of total pressure. Indeed, the drop in the total pressure, averaged on the yz plane,

998 A12-20

between the inflow and outflow surfaces in the presence of the microramp is 0.82 % smaller than that without control.

4.4. *Vortical structures: a mean view*

An interesting issue regarding the effects of microramps on SBLI is the mutual interaction between the arch-like vortical structures induced by MVGs and the interaction region.

According to the literature and the results in the previous sections, the main effect on the SBLI of the arch-like vortices is that they periodically disrupt the impinging and reflected shock waves, leading to regions of large curvature in the shock surfaces (the 'bump' in figure 5). The effect of the shock waves on the arch-like vortices is instead less clear. Some works (Yan *et al.* 2013) suggest that these vortices travel rather undisturbed across the shock, however, quantitative information supporting this statement, regarding for example the effect of SBLI on the trajectory and intensity of the arch-like vortices, is lacking.

It is known from the literature (Jeong & Hussain 1995) that vorticity magnitude may be an improper measure to identify coherent vortical structures. However, as the trace of the vortices related to the microramp and the SBLI is strong enough compared to the background shear, at least in the ramp wake and in the interaction region, we consider in the following the behaviour of the Favre-averaged vorticity, defined in this work as the curl of the Favre-averaged velocity ($\tilde{\boldsymbol{\zeta}} = \nabla \times \tilde{\boldsymbol{u}}$, see Appendix B), to assess the streamwise development of these vortices. In particular, we can assume that, at the symmetry plane, the negative peaks of the spanwise component $\tilde{\zeta}_z$ correspond to the trace of the K–H vortices associated with the arch-like vortices and with the shear layer delimiting the separation (see figure 17).

Locating these minima and recording the magnitude of the vorticity along these loci allows us to track the trajectory of the main vortical structures and investigate the streamwise evolution of their intensity. Figure 18 reports the wall-normal coordinate of the points with minimal Favre-averaged spanwise vorticity for a given streamwise section, whereas figure 19 reports the corresponding value of the mean spanwise vorticity.

Observing the last figure, the peaks in correspondence with the shock position suggest an increase in the intensity of the external shear layers that directly intersect the impinging shock in both the USBLI and CSBLI cases (red and blue curves). Whether this increase is associated with the generation of vorticity induced by baroclinic, diffusive, turbulent or other effects is not clear at this stage. However, if we observe the equation for the evolution of the Favre-averaged vorticity (see Appendix B), we obtain that

$$\frac{\mathrm{D}}{\mathrm{D}t}\left(\frac{\tilde{\boldsymbol{\zeta}}}{\bar{\rho}}\right) = \left(\frac{\tilde{\boldsymbol{\zeta}}}{\bar{\rho}}\right) \cdot \nabla \tilde{\boldsymbol{u}} + \frac{\nabla \bar{\rho} \times \nabla(\bar{p} + 2/3\bar{\rho}\tilde{k})}{\bar{\rho}^3} + \frac{1}{\bar{\rho}}\nabla \times \left(\frac{\nabla \cdot \tau^{t,d}}{\bar{\rho}}\right), \qquad (4.2)$$

where the first term at the right-hand side is the compressible vortex stretching and tilting, the second term is the baroclinic term and the third term is the diffusion of vorticity by the action of viscous and turbulent stresses. We indicated with D/Dt the material derivative, and with $\tau_{ij}^t = \overline{\tau_{ij}} + \widetilde{\tau}_{ij}^R$ the total stress tensor including both the Reynolds-averaged molecular stress tensor $\overline{\tau_{ij}}$ and the Favre-averaged Reynolds stress tensor $\widetilde{\tau}_{ij}^R = -\overline{\rho u_i'' u_j''}$, while the Reynolds-averaged pressure is indicated as $\bar{p}$, the Favre-averaged turbulent kinetic energy as $\tilde{k}$ and the deviatoric part of the total stress tensor as $\tau_{ij}^{t,d}$. Compressibility effects in the conservation of mass for a generic fluid element are thus correctly accounted for in the Favre-averaged vorticity equation only if we introduce density-weighting. Indeed, by dividing the Favre-averaged vorticity by the Reynolds-averaged density, the
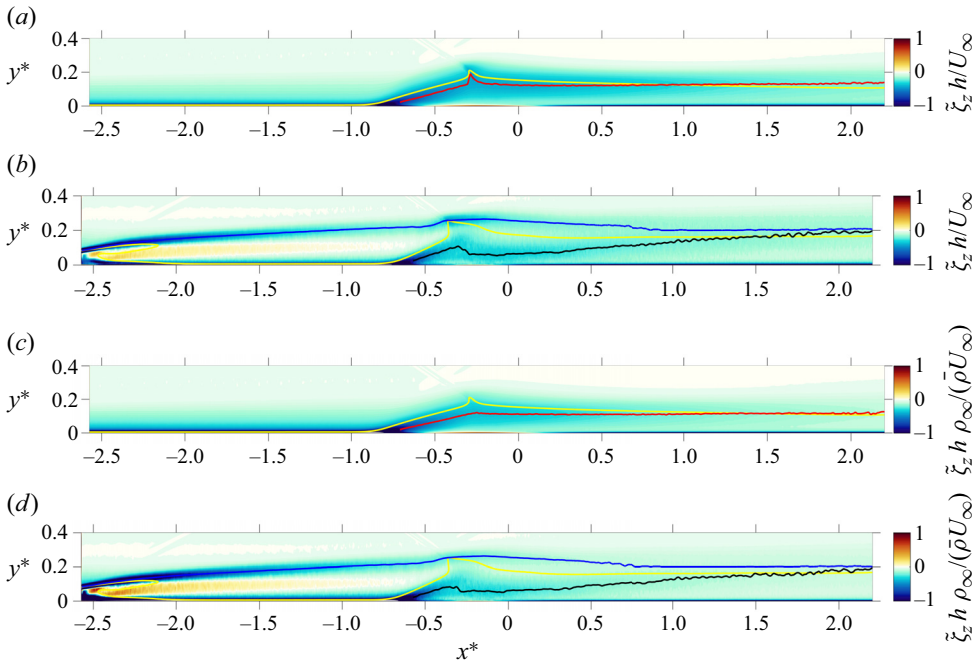
Figure 17. Contours of the spanwise component of the Favre-averaged vorticity (*a,b*) and the density-weighted Favre-averaged vorticity (*c,d*) for the USBLI (*a,c*) and the CSBLI (*b,d*) cases. Yellow lines indicate points at $\tilde{M} = 1$, blue and black lines indicate respectively the position of the top and bottom shear layers of the CSBLI case, while red lines indicate the shear layer of the USBLI case.
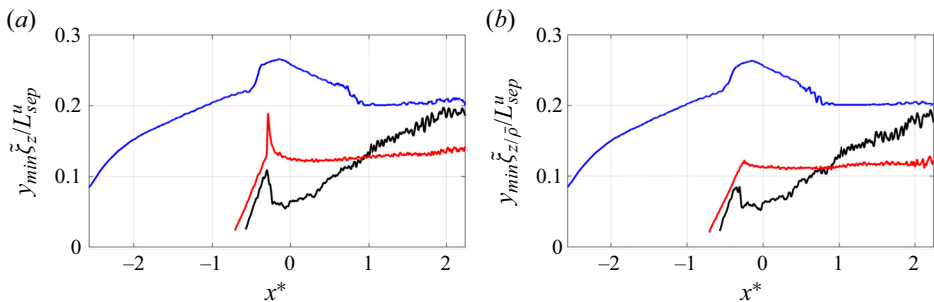

Figure 18. Wall-normal position of shear layers at the symmetry plane based on the spanwise Favre-averaged vorticity (*a*) without and (*b*) with density weighting: USBLI shear layer (red), CSBLI bottom shear layer (black) and CSBLI top shear layer (blue).

classical equations describing vorticity dynamics are recovered. Therefore, if we observe the contours of the specific vorticity $\widetilde{\zeta_z}/\bar{\rho}$ (figure 17), we can see that the sudden jump observed in correspondence with the incident shock is mainly an effect of the conservation of mass associated with the sudden density rise, which is also observable in the USBLI case. Figure 19 further confirms this conclusion, suggesting that only a limited generation of mean vorticity in the top shear layer of the CSBLI case can be related to baroclinic or turbulent effects across the shock, as the vortex stretching and tilting term is null for the spanwise vorticity component because of the flow symmetry at $z^* = 0$. Looking at the specific vorticity, the decay of the shear layer intensity is now almost undisturbed by
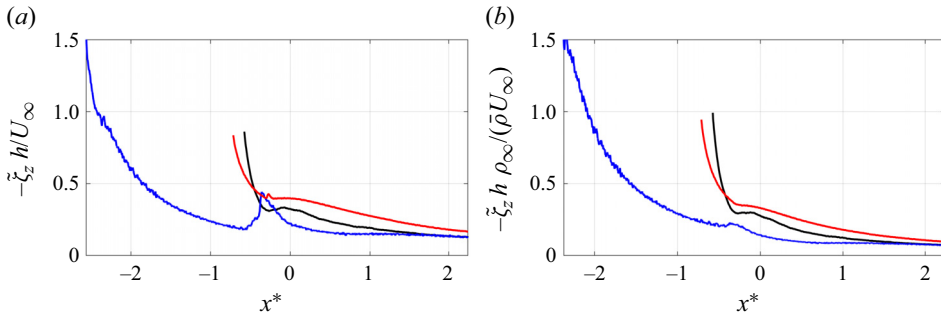
Figure 19. Spanwise component of the Favre-averaged vorticity (*a*) without and (*b*) with density weighting along the respective shear layers at the symmetry plane: USBLI shear layer (red), CSBLI bottom shear layer (black) and CSBLI top shear layer (blue).

the presence of the shock, which confirms the qualitative belief that the arch-like vortices are robust enough not to be affected by SBLI. Figure 18, however, shows that there is no relevant difference between the trajectories of the wall-normal coordinates of the $\widetilde{\zeta}_z$ and $\widetilde{\zeta}_z/\bar{\rho}$ peaks. Considering the CSBLI case, the bottom shear layer surrounding the separation region follows the behaviour of the one in the USBLI case up to reattachment ($x^* \approx 0$). Conversely, the upper shear layer defined by the arch-like vortices and delimiting the edge of the boundary layer, first rises slowly until the interaction region, because of the known lift-up at the symmetry plane in the microramp wake, and then follows the triangular shape of the separation region with a slow recover after reattachment. Indeed, the wall-normal position is affected by the separation up to $x^* \approx 1$. After the reattachment point, the bottom shear layer converges to the upper one, which thus delimits the new boundary layer downstream of the interaction, becoming significantly thicker than in the USBLI case.

4.5. *Flow unsteadiness*

Except for very few recent studies (Dong *et al.* 2018; Grébert *et al.* 2018; Sun *et al.* 2020; Grébert *et al.* 2023), the features of the flow unsteadiness associated with MVG-controlled SBLI have been scarcely considered in the literature, despite the shock low-frequency unsteadiness being one of the most critical aspects for SBLI. Indeed, long integration periods to capture this spectral property are computationally demanding for high-fidelity methods, and RANS methods are notoriously unable to properly describe flow unsteadiness. To shed light on the spectral characteristics of the flow under consideration, in the following, we analyse the time evolution of the pressure at the wall. We first present a Fourier analysis of the pressure along the *xz* and *xy* planes and then a wavelet analysis of $p_w(t)/p_\infty$ for selected probes.

4.5.1. *Spectra*

Streamwise spectra. First, we consider the overall picture given by the spanwise-averaged premultiplied spectra of the wall pressure along the streamwise coordinate. Spectra have been evaluated with the Welch method, using 16 (USBLI) and 8 (CSBLI) segments with 50 % overlap and a rectangular window, and have then been smoothed using a Konno–Ohmachi filter (Konno & Ohmachi 1998). A summary of the main results is reported in table 4, where x^*_{low} is the location of the low-frequency peak, x^*_{sep} is the separation point, x^*_{peak} is the foremost wall-pressure standard deviation peak, x^*_{reat} is the

Case	x^*_{sep}	x^*_{low}	x^*_{peak}	L_{sep}/δ_{shk}	$f\,L^u_{sep}/U_\infty$	$f\,L_{sep}/U_\infty$
USBLI (spanwise-averaged)	−0.838	−0.792	−0.779	4.994	0.052	0.052
CSBLI (spanwise-averaged)	−0.694	−0.666	−0.626	3.672	0.079	0.058
CSBLI ($z^* \approx -0.30$)	−0.717	−0.645	−0.661	4.061	0.082	0.067
CSBLI ($z^* \approx -0.05$)	−0.659	−0.647	−0.625	3.120	0.082	0.051
CSBLI ($z^* \approx 0.00$)	−0.699	−0.642	−0.628	3.619	0.079	0.057

Table 4. Main streamwise locations of interest, separation length and value of the peak low frequency.

reattachment point, L_{sep}/δ_{shk} is the separation length with respect to the boundary layer thickness at inviscid shock impingement, $f\,L^u_{sep}/U_\infty$ is the non-dimensional value of the peak low frequency with respect to the free-stream velocity and the USBLI separation length and $f\,L_{sep}/U_\infty$ is the non-dimensional value of the peak low frequency with respect to the free-stream velocity and the local separation length.

The contours in figure 20 show the typical behaviour of the wall-pressure spectra. A broadband low-frequency peak in correspondence with the onset of the separation is associated with the oscillations of the separation shock foot. The low-frequency peak is followed by an intermediate region with mid-to-high frequencies associated with the development of the separation bubble. Here, the dominant frequencies drop in the first half of the bubble and then rise in correspondence with the reattachment. After this point, high-frequency pressure fluctuations indicate the increased turbulent activity in the boundary layer following the interaction. In the CSBLI case, we can also notice a high-frequency content before the interaction onset due to the microramp wake flow. The energetic region, sharp in space at $x^* \approx -2.4$ and broadband in frequency, corresponds to the peak of the wall-pressure standard deviation observed just after the ramp trailing edge (see figure 8) and is associated with the trace on the wall of the conical shock around the microramp wake (Della Posta *et al.* 2023). Comparing the USBLI and CSBLI cases, we can notice that the entire frequency content is slightly shifted towards higher frequencies. As a result, the low-frequency broadband peak, whose absolute maximum is located at $f\,L^u_{sep}/U_\infty \approx 0.052$ for the USBLI case, increases slightly up to $f\,L^u_{sep}/U_\infty \approx 0.079$ for the CSBLI case. Similar values were obtained from LES data in Grébert *et al.* (2023), with the maximum low-frequency activity concentrated around $f\,L^u_{sep}/U_\infty \approx [0.03, 0.05]$ and not significantly affected by the MVGs. In addition, another low-frequency energetic content is visible at $x^* \in [-0.5, -0.25]$, where the second peak of wall-pressure standard deviation is present in figure 8. This interval corresponds to the first half of the interaction, where the height of the separation bubble is increasing and the impinging shock interacts with the shear layer surrounding the recirculating flow. Finally, although an increased energy content is observable at $f\,L^u_{sep}/U_\infty \in [3, 4]$, corresponding to the shedding frequency of the arch-like vortices (Bo *et al.* 2012; Della Posta *et al.* 2023*a*), we cannot conclude that this is a trace on the wall of these structures, as an analogous increase at the same frequencies is also observable in the uncontrolled case.

Given the relevant spanwise modulation of the flow induced by the microramp, it is worth considering the premultiplied spectra along the streamwise direction at single spanwise sections. As in the previous sections, we examine the notable stations at $z^* \approx -0.3, -0.05$ and 0. Figure 21 shows that there is no qualitative distinction between the spectra in the span and also the low-frequency peak takes place at approximately the same Strouhal number. Slight quantitative differences however are present in the reattachment region and beyond ($x^* \approx [-0.25, 0.5]$) for high frequencies ($f\,L^u_{sep}/U_\infty \in [2, 5]$). At $z^* \approx$
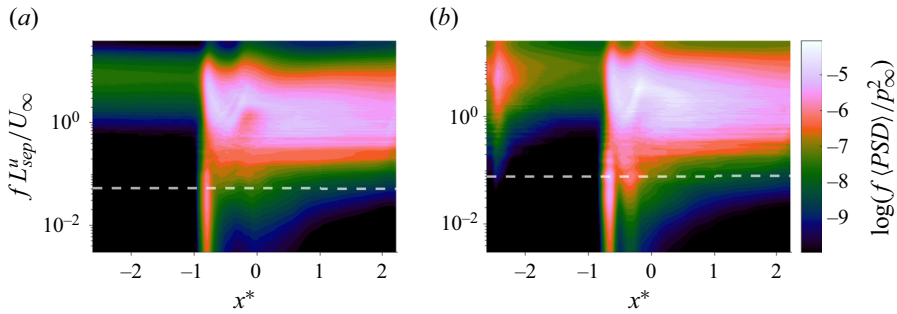
Figure 20. Streamwise distribution of the spanwise-averaged premultiplied wall-pressure spectra: (*a*) USBLI and (*b*) CSBLI. The dashed white line indicates the frequency of the low-frequency peak in the shock region.

-0.05, the intensity of the spectra is higher, suggesting an increased activity of the eddies in the boundary layer. In this section, the local separation length is minimum and the height of the recirculation bubble is smaller (see figure 12). Given this observation, we could speculate that the action of the arch-like vortices, whose characteristic shedding frequency is precisely in this range, is here felt stronger close to the wall and thus contributes to the surge in the spectra. Moreover, looking at the distribution of the skin friction lines in figure 11, the spanwise section with minimum separation length corresponds approximately to the location of a focus on the reattachment line, where the convergence of the flow could further contribute to the observed increase in high-frequency wall-pressure fluctuations. Unsteady data in this spanwise section have not been considered in this work and will be the subject of future research. An increased intensity is also visible close to the ramp trailing edge at $z^* \approx -0.05$. Here, at the sides of the primary vortex pair, the conical shock wave around the microramp wake can penetrate the flow close to the wall, thus leaving a stronger imprint on the spectra.

Finally, it is worth noting that, despite its increase in absolute terms, if the local peak frequency is scaled by the local separation length (table 4), the resulting non-dimensional frequency goes back approximately to the value of the 2-D USBLI. The slight differences that are still present may be due to 2-D issues that make the 2-D scaling not completely effective.

Spanwise spectra. To better investigate the relative distribution in frequency in the z^* direction, figure 22 reports the premultiplied spectra along notable curves in the span. The previous analysis confirmed that the microramp wake modulates the flow in the spanwise direction, with a mild variation also in the spectral features of the SBLI. For this reason, to compare analogous conditions along z^*, we sampled the wall-pressure signals following the separation line, the foremost wall-pressure standard deviation peak location, and the reattachment line (see figure 11*c*). However, the integral in frequency of the spectra is not constant along these curvilinear coordinates, as it corresponds to the variance of the local wall-pressure signals (Parseval's theorem), which changes along the xz plane in the CSBLI case. Since we want to compare only the relative distribution in frequency at different sections, we normalised the spectra with the local wall-pressure variance. The results allow us to examine how the relative magnitude of the spectral content associated with the shock oscillation, turbulent fluctuations and other features varies along the span.

From the contours in the first row, as expected, the USBLI results show that the relative distribution is approximately constant along the span. Along the (straight) separation line, the energy of the wall-pressure signal is distributed evenly between the low- and high-frequency ranges. Moving downstream, towards the standard deviation peak and
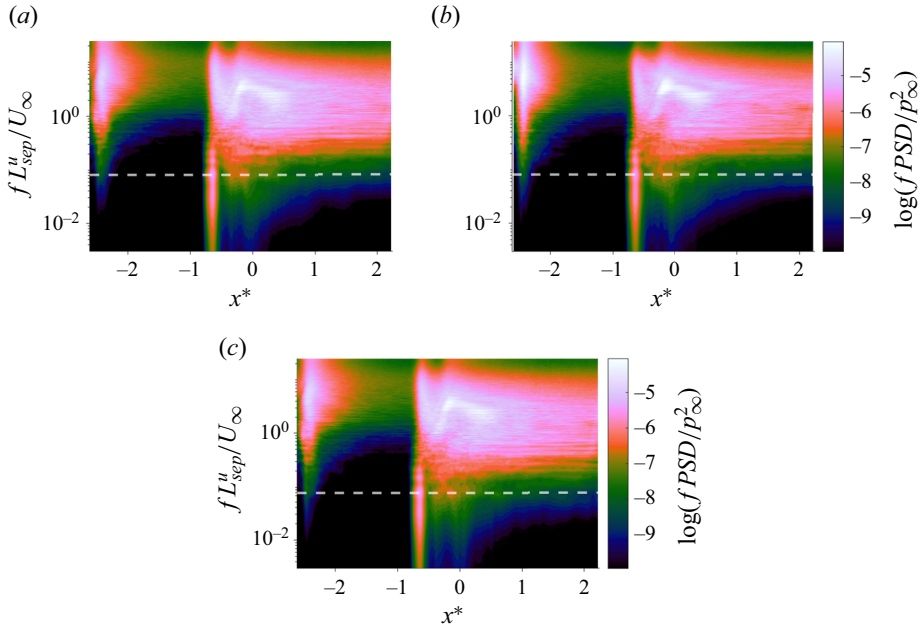
998 A12-25

(*a*)

(*b*)

(*c*)

Figure 21. Streamwise distribution of the premultiplied wall-pressure spectra of the CSBLI case at: (*a*) $z^* \approx -0.3$, (*b*) $z^* \approx -0.05$ and (*c*) $z^* \approx 0$. The dashed white line indicates the frequency of the local low-frequency peak in the shock region.
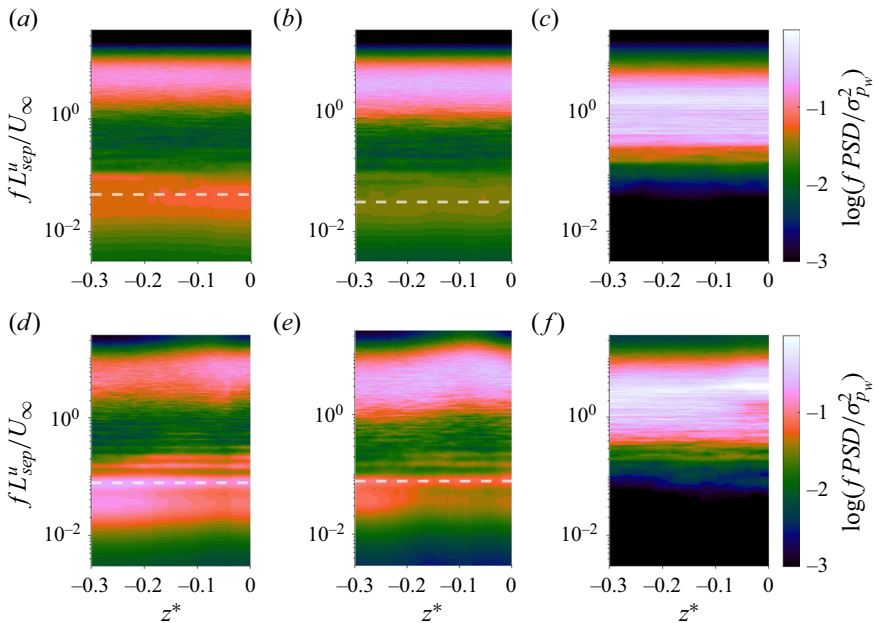
(*a*)

(*b*)

(*c*)

(*d*)

(*e*)

(*f*)

Figure 22. Spanwise distribution of locally normalised premultiplied wall-pressure spectra: USBLI (*a–c*) and CSBLI (*d–f*), along the separation (*a,d*), along the wall-pressure standard deviation peak (*b,e*), and along the reattachment (*c,f*).

998 A12-26

then the reattachment (straight) lines, the dominant spectral content shifts to higher frequencies, as the influence of the reflected shock unsteadiness vanishes progressively. At the reattachment, the peak frequency related to the eddies in the reattaching boundary layer is $f L^u_{sep}/U_\infty \approx 2$.

The contours of the second rows report, instead, the results of the CSBLI case. Along the separation, compared with the USBLI case, the scenario at the side and central regions is different. Close to the lateral boundaries, the energy of the signal at the low-frequency peak is larger than the energy at high frequencies. The opposite takes place at the centre of the domain, behind the microramp, where the contribution from the low frequencies is dampened and the high-frequency contributions are stronger. According to the previous results, the spectra in the span confirm that although microramps do not cancel the global unsteadiness of the shock, they provide a local attenuation of its relative impact in the region of their wake. Moreover, as the frequency associated with the shock unsteadiness stays almost constant, we can deduce that, despite its geometry being altered by the impingement of the ramp wake, the front of the reflected shock remains coherent in the span during its low-frequency oscillation. The distribution along the peak standard deviation is similar to that along the separation, although we note that the contribution from the low-frequency range in the CSBLI case is still relevant compared with the USBLI case. In both figures 22(*d*) and 22(*e*), we also note a mild shift towards higher frequencies close to the symmetry plane. Although there may be effects associated with the local reduction of the separation extent, we can speculate that the shift in value of the high-frequency content is primarily due to the different streamwise positions of the loci considered along the spanwise direction. Indeed, the inner portion of the separation line and of the wall-pressure standard deviation peak in the CSBLI case are generally more downstream, where high-frequency turbulent fluctuations count more. Interesting differences are present instead along the reattachment line. Similarly to the USBLI case, the energy is here concentrated in the high-frequency range, and especially at the lateral boundaries the contour is almost the same as without microramp. However, close to the symmetry plane, the dominant contribution increases slightly in magnitude and frequency, reaching exactly the shedding frequency of the arch-like vortices in a peaked fashion.

A trace at the wall of the K–H vortices around the wake is noticeable only at the reattachment, while the typical tonal signature at $f L^u_{sep}/U_\infty \in [3, 4]$ is absent in the first part of the interaction. Considering also their reduced spanwise vorticity compared with that of the bottom shear layer (see figure 19), it is possible to believe that the action of the arch-like vortices is first shielded by the 3-D shear layer developing around the separation region, and thus that they may play a limited role in the delay of the separation. Their role may instead be more relevant in the mechanism to close the recirculation bubble.

Wall-normal spectra. We complete the picture of the Fourier analysis with figure 23, which shows the premultiplied spectra of the pressure along the wall-normal coordinate, at the symmetry plane. Time signals are sampled in correspondence with a streamwise location close to separation (*a,b*) and reattachment (*c,d*) for the USBLI (*a,c*) and CSBLI (*b,d*) cases. These spectra allow us to locate the characteristic frequencies of the flow in the wall-normal direction, and thus relate the behaviour of the fluctuations at the wall with those far from the wall.

The USBLI results at the separation document the energetic fluctuations associated with the low-frequency motion of the reflected shock wave, which initiates the separation penetrating the boundary layer up to a short wall-normal distance. The high-frequency content close to the wall is instead the trace of the vortical structures living at the edge of the recirculation bubble. Indeed, their intensity is small at separation, as the separation
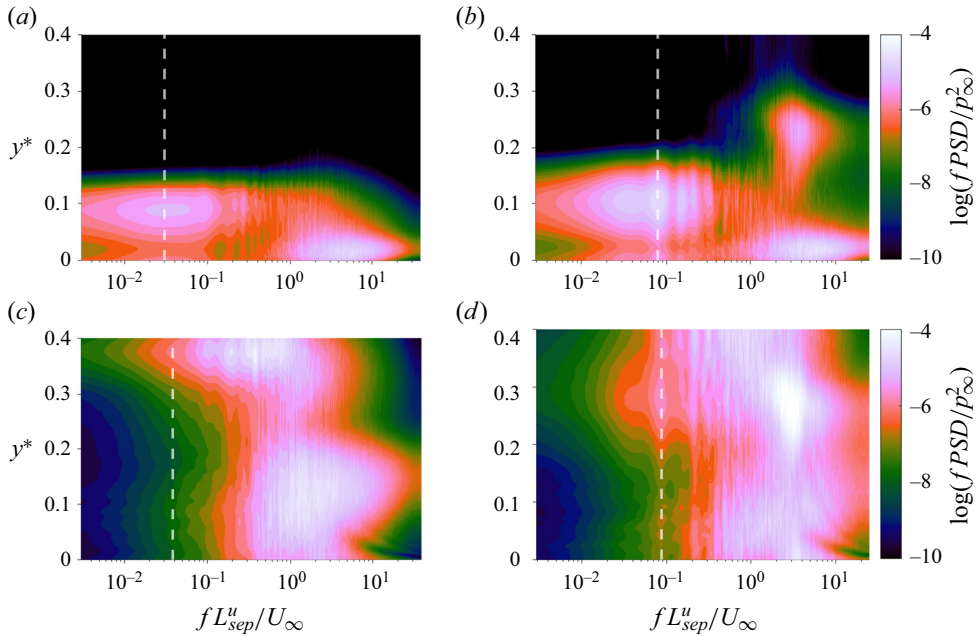
Figure 23. Wall-normal distribution of the premultiplied wall-pressure spectra at the symmetry plane in the (*a*,*b*) separation and (*c*,*d*) reattachment regions. USBLI on (*a*,*c*) and CSBLI on (*b*,*d*). The dashed white line indicates the local low-frequency peak associated with the oscillation of the separation shock.

shear layer is here still at its onset, while being diffused across the vertical direction at reattachment, where pressure fluctuations are associated with the eddies of the new boundary layer downstream of the interaction. Finally, the contour at reattachment shows also an interesting feature related to the reattachment shock taking place downstream of the separation, observable at $y^* \approx 0.38$. This shock is characterised by a broadband shape, as for the separation shock, despite its peak non-dimensional frequency being considerably higher (at least a decade more than the traditional low-frequency unsteadiness).

The CSBLI contours show analogous results for what concerns the trace of the low-frequency peak of the separation shock, although the trace now covers a larger wall-normal range, suggesting an increased shock smearing.

The most interesting difference, however, is the strong peak at $y^* \in [0.2, 0.3]$ and $f L^u_{sep}/U_\infty \in [2, 5]$, which marks the spectral content of the arch-like vortices. This contribution remains generally separate from the high-frequency one located close to the wall, especially in the separation region, and its intensity is comparable with that of the most energetic features in the spectra. At reattachment, the rise in intensity of the fluctuations in the high-frequency range induced by the shocks all along the wall-normal direction causes a larger peak in correspondence with the arch-like vortices, whose influence is able to reach the wall, as we observed in the spanwise spectra reported in figure 22(*f*). The spectral analysis thus confirms that the arch-like vortices' shedding frequency is in the same range as the turbulent fluctuations taking place in traditional SBLI and that their influence directly reaches the wall only at reattachment. However, despite providing interesting information about the spatial and spectral features of the flow, spectra do not provide information about the actual reattachment mechanism in microramp-controlled SBLIs and about the role arch-like vortices play in it, which thus remains an open question for future work.

998 A12-28

4.5.2. *Wavelet analysis*

In this section, we want to characterise the degree of intermittency of the wall-pressure signals in the interaction region, in particular at the onset of the separation and at reattachment. Similarly to the approach adopted in Bernardini *et al.* (2023*a*), wavelet analysis is applied to extract energetic intermittent events. Indeed, this approach provides a more direct measure of the degree of intermittency of the wall-pressure field and allows for the extraction of local (in time) features that may be partially lost using Fourier analysis.

The wavelet transform is computed by the convolution of the wall-pressure signal $p_w(t)$ with the dilated (by the factor k) and translated (by the factor t) complex conjugate counterpart of a so-called mother wavelet, according to the following formalism:

$$G_\Psi(k, t) = \frac{1}{\sqrt{k}} \int_{-\infty}^{+\infty} p_w(\tau) \Psi^* \left(\frac{\tau - t}{k} \right) \, \mathrm{d}\tau, \qquad (4.3)$$

where Ψ is the wavelet mother function, k is a dilatation parameter indicating the time scale of the event under consideration, t is the time-translation parameter and $*$ denotes the complex conjugate. A detailed theoretical framework can be found in Farge (1992) and Mallat (1999). In this study, the Morlet wavelet has been chosen, as a higher resolution in frequency can be achieved compared with other mother functions. Owing to the wavelet admissibility condition (Torrence & Compo 1998), the frequency associated with the dilatation parameter for the Morler wavelet is defined as $f = 0.97/k$. Scalograms of the wall pressure at separation and reattachment on the symmetry plane for the two cases are reported in Appendix C.

In statistics, intermittency denotes the rare occurrence of exceptionally spiky events which are patchy and bursty. These instances cause higher-order moments (skewness and flatness) to converge with greater difficulty, suggesting a significant departure from Gaussian statistics and, hence, non-homogeneous distribution of energy in time (Camussi & Bogey 2021).

Once computed the wavelet transform coefficients $G_\Psi(k, t)$, it is possible to obtain the scale-time distribution of the energy density $|G_\Psi(k, t)|^2$ of the wall-pressure signal. Thanks to this property, Meneveau (1991) and Camussi & Bogey (2021) suggested that an effective indicator of the intermittency is the squared local intermittency measure, denoted as *LIM*2:

$$LIM2(k, \tau) = \frac{|G_\Psi(k, t)|^4}{\langle |G_\Psi(k, t)|^2 \rangle_t^2}, \qquad (4.4)$$

where $\langle \bullet \rangle_t$ indicates the time average of the considered quantity. *LIM*2 can be interpreted as a time-scale dependent measure of the flatness factor or kurtosis of wall-pressure signals. Therefore, the *LIM*2 parameter will be equal to 3 when the probability distribution is Gaussian, while the condition *LIM*2 > 3 identifies only those rare bursts of energy contributing to the deviation of the wavelet coefficients from a normal, Gaussian distribution.

In the following, we apply the wavelet analysis to the wall-pressure signal at two relevant stations for both the USBLI and CSBLI cases: the separation point and the reattachment point at the symmetry plane. Figure 24(*a*) shows the LIM2 maps (only the levels greater than 3) at the separation point for USBLI. The occurrence of intermittent events in the frequency range characterising the shock unsteadiness, whose Fourier frequency peak is indicated with a dashed horizontal line, is immediately apparent. The most relevant characteristic feature of these bursts of energy is that they are rather scattered in time and clustered around the Fourier peak frequency, but with some very energetic events at
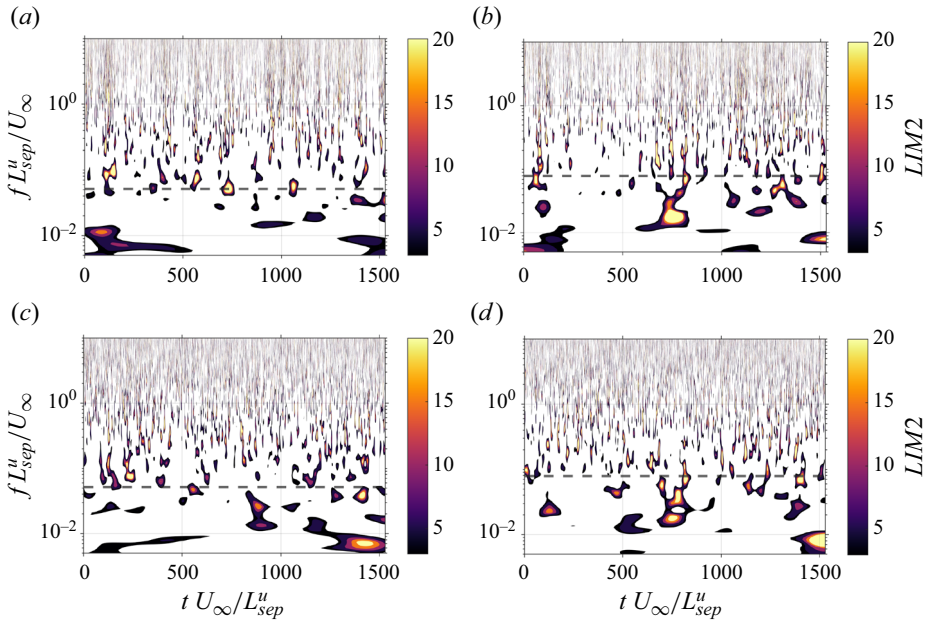
Figure 24. Contours of *LIM*2 of p_w/p_∞ at the separation (*a,b*) and reattachment points (*c,d*) at the symmetry plane. USBLI (*a,c*) and CSBLI (*b,d*). Only *LIM*2 values above 3 are shown. Dashed black lines indicate the dominant low-frequency peak of each case.

lower frequencies. The long simulation time allows our DNS to capture these rare events. This picture again confirms that the low-frequency unsteadiness of SBLIs is composed of a collection of energetic events, whose rarity causes the difficulty of convergence of higher-order statistics. Nevertheless, it is important to underline that the computational time is largely sufficient to evaluate the means and the variances of the wall-pressure signals, as well as the Fourier spectra, as amply demonstrated in the literature (Touber & Sandham 2009; Bernardini *et al.* 2023*a*). Indeed, we verified that relative standard errors, evaluated using the bootstrap method (Efron & Tibshirani 1994), for the mean and variance at separation and reattachment on the symmetry plane are smaller than 1 %. At higher frequencies, it is possible to see the intermittency given by turbulence which is quite separate in the frequency space from the events caused by the shock/boundary layer interaction. If we now look at the CSBLI case in figure 24(*b*), it is evident that the intermittent events are grouped around a higher frequency, as indicated by the Fourier analysis, with the additional occurrence of a single extremely energetic low-frequency event at $tL^u_{sep}/U_\infty \approx 750$. The analysis of the LIM2 maps at the reattachment points for both cases, figures 24(*c*) and 24(*d*), shows a very similar behaviour. We can just note that the energetic bursts at lower frequencies survive for all the interaction length. It may be concluded therefore that, at least for these test case conditions, microramps do not alter significantly the highly intermittent nature of SBLI.

5. Conclusions

Given the increased interest in manoeuvrable aerospace systems flying at supersonic and hypersonic speeds, studying possible control strategies to remedy the adverse effects of often occurring SBLIs is crucial. A promising strategy to reduce the boundary layer

separation induced by an impinging shock is the use of MVGs, sub-boundary layer passive vortex generators able to retard the separation. Although several studies described many aspects of the mean and instantaneous features induced by MVGs, also in the presence of SBLIs, many questions remain open, regarding for example the organisation of the K–H vortices in the MVG wake and their interplay with SBLIs, the topology of the interaction region, the effect of MVGs on the shock dynamics and its intermittency, and the effect of relevant flow and geometrical parameters. Moreover, only a few studies have used experimental or numerical methodologies that can provide reliable, high-fidelity data with full accessibility of the results like DNSs do, which is especially worthy for such a 3-D and unsteady wall flow such as that under consideration. Indeed, DNSs provide the research community with fine-resolved reference data and with a fruitful chance to explore features that cannot be considered, or may be misrepresented otherwise, and that for this reason have been scarcely considered in the literature despite their relevance, e.g. unsteady instantaneous properties or spectral attributes.

Given this scenario, this study uses DNSs to examine the effects of a ramp-type MVG on the flow physics of a classical SBLI generated by an oblique shock wave impinging on a turbulent boundary layer over a flat plate. In particular, we compare a baseline simulation considering an uncontrolled SBLI, named USBLI, with another considering a microramp-controlled SBLI, named CSBLI, whose geometrical set-up is based on the optimisation study of Anderson *et al.* (2006). A remarkably long integration period is considered for both cases, allowing us to examine the effects of microramps on the characteristic low-frequency unsteadiness of SBLIs.

A qualitative analysis of the results shows that, besides two additional shocks, the microramp induces a significant spanwise modulation of the flow. Alternated regions of accelerated and decelerated flows retard the separation depending on the span location, and large-scale streak structures associated with the ramp wake overlap the boundary layer streaks typically observed in wall-bounded turbulent flows, even after the interaction. Bumps in the separation shock surface are also generated by the periodic impingement of the arch-like vortices around the ramp wake, which are clearly visible in the billows at the symmetry plane not only upstream of the interaction but also far downstream.

The mean wall pressure shows that the onset of separation is effectively shifted downstream, with a corresponding increase in the overall pressure gradient across the interaction. Despite what is typically observed for 2-D flows, where the onset of separation is relatively insensitive to changes in shape factor (the H-paradox, Babinsky & Harvey 2011), the fuller (3-D) boundary layer induced by the microramp wake upstream of the interaction successfully reduces the separation length in the case under consideration. Indeed, although the mean wall pressure is approximately constant along the span, the streamwise distributions of the wall-pressure standard deviation and of the time-averaged streamwise skin friction coefficient confirm that the flow cannot be studied using traditional tools used for 2-D SBLIs because of the non-negligible three-dimensionality of the flow, even far from the wall. Finally, corresponding to an overall decrease in the separation length and an increase in the pressure gradient, the intensity of the pressure fluctuations increases, as already observed in transitional SBLIs and SBLIs on non-adiabatic walls, suggesting a common process or mechanism that deserves attention.

The analysis of the mean skin friction lines provides then valuable information to fully comprehend the changes in the separation bubble, whose topology is largely 3-D. For example, the convergence of the lines into critical loci on the wall indicates the formation of tornado-like structures redistributing the flow in both the wall-normal and transversal directions. The confluence and departure of the lines at the forefront and rear parts of the interaction allowed us to identify the separation and reattachment line, respectively,

and thus to estimate the precise variation along the span of the streamwise separation length. The CSBLI case shows a mean separation shorter than 30 % the value of the USBLI case but presents variations of up to 30 % along the span compared with the mean value. Moreover, thanks to the analysis of the added momentum (Giepman *et al.* 2014), we show that the region of minimum separation is strictly associated with that of maximum momentum transport towards the wall by the helical motion of the ramp wake. The transport retards the separation and also has a slight beneficial effect in terms of total pressure recovery compared with the uncontrolled case, but induces an increase in skin friction, which adds to the drag force on the microramp itself. We note, moreover, that the effects of the primary vortices and the spanwise non-uniformity of the flow last even far downstream of the interaction, which, for example, may be inconvenient for the components following the separation in supersonic inlets. Predicting how long these effects last is also a relevant question, as it may directly impact the design of the devices and their positioning.

Another debated aspect we deal with is the characterisation of the mutual interaction between the arch-like vortices and the interaction region. The distribution of spanwise vorticity at the symmetry plane allowed us to examine the effects of the interaction on the vortices and shows that the trajectory of the arch-like vortices follows the edge of the separation. Their intensity, instead, is almost unaffected by the shocks if one accounts correctly for compressibility effects by considering a density scaling of the vorticity defined with the Favre-averaged velocity, following our analytical derivation. On the other hand, we show that the arch-like vortices directly affect the interaction by periodically altering the shape of the separation shock. In addition, the spectral analysis in the streamwise, spanwise and wall-normal directions, shows that a trace in the wall pressure of the K–H shedding frequency defined by Bo *et al.* (2012) and Della Posta *et al.* (2023*a*) is only visible at reattachment. Results thus suggest that the arch-like vortices may be less relevant for the separation delay, although their role in the unsteady closure of the bubble is still unrecognised and deserves further study.

We then present a thorough and original analysis of the Fourier spectra in the streamwise direction, in the spanwise direction following the separation and the reattachment lines and in the wall-normal direction at the separation and reattachment at the symmetry plane. Results show that microramps induce an increase in the magnitude and the non-dimensional frequency, scaled by the separation length of the USBLI case, of the typical low-frequency SBLI unsteadiness. The rise is approximately constant along the span, although the relative contribution of the low-frequency fluctuations is attenuated behind the ramp compared with what happens at the lateral boundaries. Results thus indicate that, although the arch-like vortices periodically modify its shape, the separation shock front oscillates coherently at the increased frequency. The physical explanation for this increase in absolute terms may be related to existing models of SBLI low-frequency unsteadiness and will be the topic of future work. However, we also highlight that, despite the three-dimensionality of the interaction, using the local separation length to make the frequency non-dimensional is still effective in recovering the typical peak low frequency.

Finally, we also used wavelet analysis to characterise how microramps affect the intermittency of the wall-pressure signal at separation and reattachment using the *LIM*2, which is a time-frequency decomposition of the flatness factor. Results show that there are no particular differences between the controlled and the uncontrolled cases, even if we observe that an even longer time integration period may be necessary to detect the differences in the higher-order statistics because of the significant intermittency of the flow also at low frequencies.
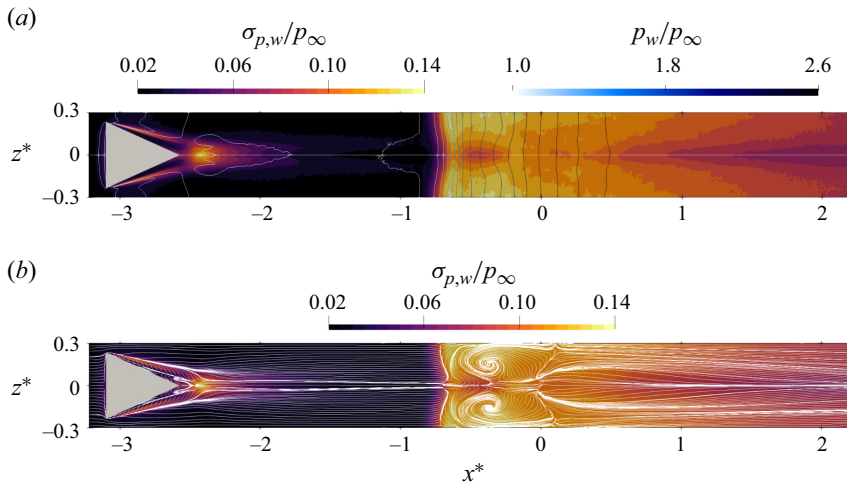
Figure 25. Contour of the wall-pressure standard deviation on the entire xz plane with (a) isolines at constant mean wall pressure (an horizontal line indicates the symmetry plane at $z^* = 0$) and (b) with skin friction lines.

Author ORCIDs.
G. Della Posta https://orcid.org/0000-0001-5516-9338;
E. Martelli https://orcid.org/0000-0002-7681-3513;
F. Salvadore https://orcid.org/0000-0002-1829-3388;
M. Bernardini https://orcid.org/0000-0001-5975-3734.

Appendix A. Symmetry of the mean flow field

Figure 25(a) shows the distribution of the mean wall pressure and of the wall-pressure standard deviation for the entire xz plane in the microramp and interaction region. From the figure it is possible to see that the mean flow can be considered as symmetric with respect to the mid-plane to a good approximation, which justifies the assumption adopted in the study.

We also report the organisation of the skin friction lines for the entire xz plane in figure 25(b), which also confirms that the overall flow topology can be described

effectively by looking at half of the domain in the spanwise direction only, although the organisation of the topology at the end of the interaction region close to the symmetry plane remains elusive, despite the long integration period considered, and thus demands further research.

Appendix B. Time evolution of the density-weighted Favre-averaged vorticity

If we define the Favre average of a generic variable ϕ as $\tilde{\phi} = \overline{\rho \phi}/\bar{\rho}$, and we average the governing equations, the conservation of mass and momentum without external forces can be written as

$$\frac{\partial \bar{\rho}}{\partial t} + \nabla \cdot (\bar{\rho}\,\tilde{\boldsymbol{u}}) = 0 \quad \Rightarrow \quad \frac{\mathrm{D}\bar{\rho}}{\mathrm{D}t} = 0, \tag{B1a}$$

$$\frac{\partial \bar{\rho}\,\tilde{\boldsymbol{u}}}{\partial t} + \nabla \cdot (\bar{\rho}\,\tilde{\boldsymbol{u}}\,\tilde{\boldsymbol{u}}) = \nabla \cdot (\bar{\tau} + \tilde{\tau}^R) \quad \Rightarrow \quad \frac{\mathrm{D}\bar{\rho}\,\tilde{\boldsymbol{u}}}{\mathrm{D}t} = \nabla \cdot \tau^t, \tag{B1b}$$

where $\mathrm{D}/\mathrm{D}t$ indicates the material derivative, $\tau_{ij}^t = \overline{\tau_{ij}} + \tilde{\tau}_{ij}^R$ is the total stress tensor including both the Reynolds-averaged molecular stress tensor $\overline{\tau_{ij}}$ and the Favre-averaged Reynolds stress tensor $\tilde{\tau}_{ij}^R = -\overline{\rho u_i'' u_j''}$. By exploiting the conservation of mass, the momentum equation can be written in non-conservative form as

$$\bar{\rho}\frac{\mathrm{D}\tilde{\boldsymbol{u}}}{\mathrm{D}t} = \nabla \cdot \tau^t. \tag{B2}$$

By taking the curl of the derived equation divided by $\bar{\rho}$, considering that $\nabla \cdot (\nabla \times \phi) = 0$ and the relation derivable using the Levi-Civita tensor for two generic vectors $\boldsymbol{a}$ and $\boldsymbol{b}$

$$\nabla \times (\boldsymbol{a} \times \boldsymbol{b}) = \boldsymbol{b} \cdot \nabla \boldsymbol{a} + \boldsymbol{a}\nabla \cdot \boldsymbol{b} - \boldsymbol{b}\nabla \cdot \boldsymbol{a} - \boldsymbol{a} \cdot \nabla \boldsymbol{b}, \tag{B3}$$

we obtain that

$$\frac{\mathrm{D}\tilde{\boldsymbol{\xi}}}{\mathrm{D}t} = \tilde{\boldsymbol{\xi}} \cdot \nabla \tilde{\boldsymbol{u}} - \tilde{\boldsymbol{\xi}}\nabla \cdot \tilde{\boldsymbol{u}} + \frac{\nabla \bar{\rho} \times \nabla (\bar{p} + 2/3\,\bar{\rho}\,\tilde{k})}{\overline{\rho}^2} + \nabla \times \left(\frac{\nabla \cdot \tau^{t,d}}{\bar{\rho}}\right), \tag{B4}$$

where we indicate with $\boldsymbol{\zeta}$ the Favre-averaged vorticity, with $\bar{p}$ the Reynolds-averaged pressure, with $\tilde{k}$ the Favre-averaged turbulent kinetic energy equal to half the trace of the Favre-averaged Reynolds stress tensor and with $\tau^{t,d}$ the deviatoric part of the total stress tensor given by $\tau_{ij}^{t,d} = \tau_{ij}^t - (\bar{p} + 2/3\,\bar{\rho}\,\tilde{k})\delta_{ij}$ neglecting bulk viscosity.

Using the expression of the mean divergence from the conservation of mass in non-conservative form

$$\nabla \cdot \tilde{\boldsymbol{u}} = -\frac{1}{\bar{\rho}}\frac{\mathrm{D}\bar{\rho}}{\mathrm{D}t}, \tag{B5}$$

we can write

$$\frac{\mathrm{D}\tilde{\boldsymbol{\xi}}}{\mathrm{D}t} + \tilde{\boldsymbol{\xi}}\,\nabla \cdot \tilde{\boldsymbol{u}} = \bar{\rho}\frac{\mathrm{D}}{\mathrm{D}t}\left(\frac{\tilde{\boldsymbol{\xi}}}{\bar{\rho}}\right), \tag{B6}$$

which substituted into (B4) gives the equation of conservation for the density-weighted Favre-averaged vorticity

$$\frac{\mathrm{D}}{\mathrm{D}t}\left(\frac{\tilde{\boldsymbol{\xi}}}{\bar{\rho}}\right) = \left(\frac{\tilde{\boldsymbol{\xi}}}{\bar{\rho}}\right) \cdot \nabla \tilde{\boldsymbol{u}} + \frac{\nabla \bar{\rho} \times \nabla (\bar{p} + 2/3\,\bar{\rho}\,\tilde{k})}{\overline{\rho}^3} + \frac{1}{\bar{\rho}}\nabla \times \left(\frac{\nabla \cdot \tau^{t,d}}{\bar{\rho}}\right), \tag{B7}$$

where the first term is the compressible vortex stretching and tilting, the second term is the baroclinic term due to modified pressure gradients and the third term is the diffusion of vorticity by the action of both viscous and deviatoric, anisotropic turbulent stresses.

The $\tilde{\zeta}$ variable that we improperly called *Favre-averaged vorticity* is actually equal to the curl of the Favre-averaged velocity. The quantity so defined is easy to evaluate and allowed us to derive an equation for the specific Favre-averaged vorticity, starting from the mass-averaged momentum equation, that is formally equal to the instantaneous specific vorticity equation. However, it is possible to show that $\tilde{\zeta}$ is different than the actual vorticity averaged according to the Favre-averaging procedure, as mass-averaging does not commute with differentiation, in contrast to the Reynolds-averaging case.

In order to show this property, we can consider without loss of generality a generic variable ϕ and the Favre average of its gradient, defined as $\widetilde{\nabla\phi} = \overline{\rho\nabla\phi}/\bar{\rho}$. Using the Einstein notation, we have that

$$
\begin{aligned}
\frac{1}{\bar{\rho}}\,\overline{\rho\frac{\partial\phi}{\partial x_i}} &= \frac{1}{\bar{\rho}}\frac{\partial\overline{\rho\phi}}{\partial x_i} - \frac{1}{\bar{\rho}}\,\overline{\phi\frac{\partial\rho}{\partial x_i}} \\
&= \frac{\partial(\overline{\rho\phi}/\bar{\rho})}{\partial x_i} + \frac{\overline{\rho\phi}}{\bar{\rho}^2}\frac{\partial\bar{\rho}}{\partial x_i} - \frac{1}{\bar{\rho}}\,\overline{\phi\frac{\partial\rho}{\partial x_i}} \\
&= \frac{\partial\tilde{\phi}}{\partial x_i} + \frac{\tilde{\phi}}{\bar{\rho}}\frac{\partial\bar{\rho}}{\partial x_i} - \frac{\tilde{\phi}}{\bar{\rho}}\frac{\partial\bar{\rho}}{\partial x_i} - \frac{1}{\bar{\rho}}\,\overline{\phi''\frac{\partial\rho}{\partial x_i}} \\
&= \frac{\partial\tilde{\phi}}{\partial x_i} - \frac{1}{\bar{\rho}}\,\overline{\phi''\frac{\partial\rho}{\partial x_i}}.
\end{aligned}
\tag{B8}
$$

As we know that $\overline{\rho\,\phi''} = 0$, we also have

$$
\frac{\partial\overline{\rho\phi''}}{\partial x_i} = 0 \quad\Rightarrow\quad \overline{\phi''\frac{\partial\rho}{\partial x_i}} + \overline{\rho\frac{\partial\phi''}{\partial x_i}} = 0 \quad\Rightarrow\quad \overline{\phi''\frac{\partial\rho}{\partial x_i}} = -\overline{\rho\frac{\partial\phi''}{\partial x_i}},
\tag{B9}
$$

which together with (B8) gives

$$
\frac{1}{\bar{\rho}}\,\overline{\rho\frac{\partial\phi}{\partial x_i}} = \frac{\partial\tilde{\phi}}{\partial x_i} + \frac{1}{\bar{\rho}}\,\overline{\rho\frac{\partial\phi''}{\partial x_i}} \quad\Rightarrow\quad \widetilde{\nabla\phi} = \nabla\tilde{\phi} + \widetilde{\nabla\phi''}.
\tag{B10}
$$

At the same time, by using the Favre decomposition of ϕ and the Favre decomposition of $\nabla\phi$, we have

$$
\nabla\phi = \nabla\tilde{\phi} + \nabla\phi'' = \widetilde{\nabla\phi} + (\nabla\phi)'' \quad\Rightarrow\quad \widetilde{\nabla\phi} = \nabla\tilde{\phi} + (\nabla\phi'' - (\nabla\phi)'').
\tag{B11}
$$

Comparing the last two equations, we are finally able to obtain that the term that makes Favre averaging and differentiation not commutative can also be expressed as

$$
\widetilde{\nabla\phi''} = \nabla\phi'' - (\nabla\phi)''.
\tag{B12}
$$

Appendix C. Wavelet scalograms of the wall-pressure signals

Figure 26 reports the scalograms of the wall-pressure time signals for the probes considered in figure 23. Scalograms report the squared magnitude of the wavelet coefficients G_Ψ and correspond to a decomposition in time and frequency of the classical
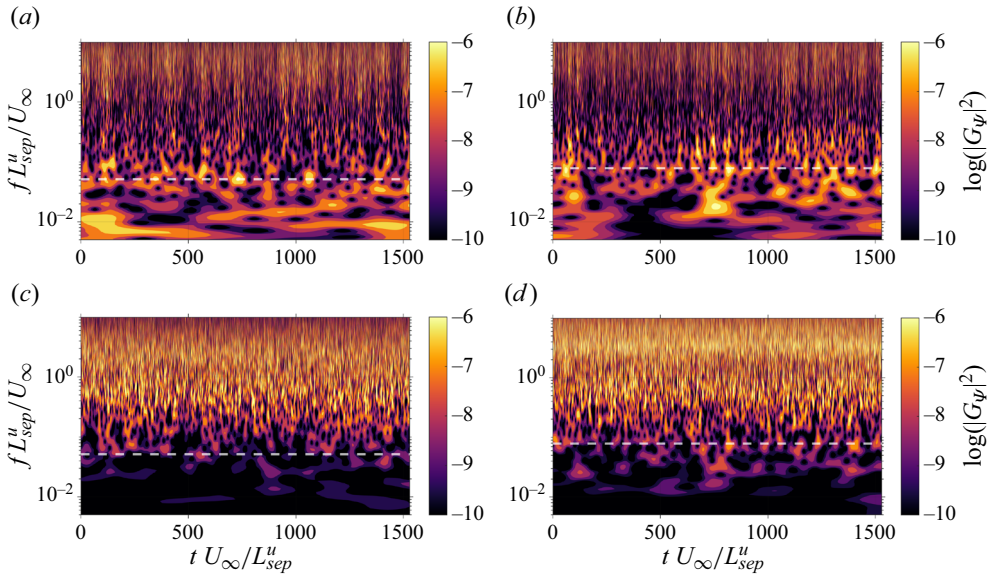
Figure 26. Scalograms of the wall pressure at (*a*,*b*) separation and (*c*,*d*) reattachment on the symmetry plane. USBLI on (*a*,*c*) and CSBLI (*b*,*d*). The dashed white line indicates the local low-frequency peak associated with the oscillation of the separation shock.

Fourier spectra. In particular, a large modulus of a wavelet coefficient indicates an intense modulation with temporal scale k of the pressure fluctuations amplitude at time τ.

The contours confirm the intermittent nature of the low-frequency shock unsteadiness and the increase in frequency of the most relevant contributions to the energy of the signal, already observed with classical Fourier analysis.

The scalograms of the controlled case also confirm the trace at high frequency of the K–H vortices seen in figures 22 and 23, which are able to leave a signature in the wall pressure only where flow reattaches and not where it separates.

REFERENCES

ADLER, M.C. & GAITONDE, D.V. 2018 Dynamic linear response of a shock/turbulent-boundary-layer interaction using constrained perturbations. *J. Fluid Mech.* **840**, 291–341.

ANDERSON, B., TINAPPLE, J. & SURBER, L. 2006 Optimal control of shock wave turbulent boundary layer interactions using micro-array actuation. In *3rd AIAA Flow Control Conf.*, p. 3197. AIAA.

BABINSKY, H. & HARVEY, J.K. 2011 *Shock Wave–Boundary–Layer Interactions*. Cambridge University Press.

BABINSKY, H., LI, Y. & FORD, C.W.P. 2009 Microramp control of supersonic oblique shock-wave/boundary-layer interactions. *AIAA J.* **47** (3), 668–675.

BERNARDINI, M., ASPROULIAS, I., LARSSON, J., PIROZZOLI, S. & GRASSO, F. 2016 Heat transfer and wall temperature effects in shock wave turbulent boundary layer interactions. *Phys. Rev. Fluids* **1**, 084403.

BERNARDINI, M., DELLA POSTA, G., SALVADORE, F. & MARTELLI, E. 2023a Unsteadiness characterisation of shock wave/turbulent boundary-layer interaction at moderate Reynolds number. *J. Fluid Mech.* **954**, A43.

BERNARDINI, M., MODESTI, D., SALVADORE, F. & PIROZZOLI, S. 2021 STREAmS: a high-fidelity accelerated solver for direct numerical simulation of compressible turbulent flows. *Comput. Phys. Commun.* **263**, 107906.

BERNARDINI, M., MODESTI, D., SALVADORE, F., SATHYANARAYANA, S., DELLA POSTA, G. & PIROZZOLI, S. 2023b STREAmS-2.0: supersonic turbulent accelerated Navier–Stokes solver version 2.0. *Comput. Phys. Commun.* **285**, 108644.

BLINDE, P.L., HUMBLE, R.A., VAN OUDHEUSDEN, B.W. & SCARANO, F. 2009 Effects of micro-ramps on a shock wave/turbulent boundary layer interaction. *Shock Waves* **19** (6), 507–520.

BNÀ, S., COLOMBO, A., CRIVELLINI, A., MEMMOLO, A., SALVADORE, F., BERNARDINI, M., GHIDONI, A. & NOVENTA, G. 2023 In situ visualization for high-fidelity CFD—Case studies. *Comput. Fluids* **267**, 106066.

BO, W., WEIDONG, L., YUXIN, Z., XIAOQIANG, F. & CHAO, W. 2012 Experimental investigation of the micro-ramp based shock wave and turbulent boundary layer interaction control. *Phys. Fluids* **24** (5), 055110.

CAMUSSI, R. & BOGEY, C. 2021 Intermittent statistics of the 0-mode pressure fluctuations in the near field of Mach 0.9 circular jets at low and high Reynolds numbers. *Theor. Comput. Fluid Dyn.* **35** (2), 229–247.

CECI, A. & PIROZZOLI, S. 2023 Natural grid stretching for DNS of compressible wall-bounded flows. *J. Comput. Phys.* **17**, 100128.

DÉLERY, J. 2013 *Three-Dimensional Separated Flow Topology: Critical Points, Separation Lines and Vortical Structures*. John Wiley & Sons.

DÉLERY, J.M. 2001 Robert Legendre and Henri Werlé: toward the elucidation of three-dimensional separation. *Annu. Rev. Fluid Mech.* **33** (1), 129–154.

DELLA POSTA, G., BLANDINO, M., MODESTI, D., SALVADORE, F. & BERNARDINI, M. 2023 Direct numerical simulation of supersonic boundary layers over a microramp: effect of the Reynolds number. *J. Fluid Mech.* **974**, A44.

DELLA POSTA, G., FRATINI, M., SALVADORE, F. & BERNARDINI, M. 2023*a* Direct numerical simulation of boundary layers over microramps: Mach number effects. *AIAA J.*, **62** (2), 542–556.

DELLA POSTA, G., MARTELLI, E., STELLA, F., BARBAGALLO, D., NERI, A., SALVADORE, F. & BERNARDINI, M. 2023*b* High-fidelity simulations of the aeroacoustic environment of the VEGA launch vehicle at lift-off. *Comput. Fluids* **263**, 105945.

DOLLING, D.S. 2001 Fifty years of shock-wave/boundary-layer interaction research: what next? *AIAA J.* **39** (8), 1517–1531.

DONG, X., YAN, Y., YANG, Y., DONG, G. & LIU, C. 2018 Spectrum study on unsteadiness of shock wave–vortex ring interaction. *Phys. Fluids* **30** (5), 056101.

DUCROS, F., FERRAND, V., NICOUD, F., WEBER, C., DARRACQ, D., GACHERIEU, C. & POINSOT, T. 1999 Large-eddy simulation of the shock/turbulence interaction. *J. Comput. Phys.* **152** (2), 517–549.

EFRON, B. & TIBSHIRANI, R.J. 1994 *An Introduction to the Bootstrap*. Chapman and Hall/CRC.

FARGE, M. 1992 Wavelet transforms and their applications to turbulence. *Annu. Rev. Fluid Mech.* **24** (1), 395–458.

GANAPATHISUBRAMANI, B., CLEMENS, N.T. & DOLLING, D.S. 2009 Low-frequency dynamics of shock-induced separation in a compression ramp interaction. *J. Fluid Mech.* **636**, 397–425.

GHOSH, S., CHOI, J.-I. & EDWARDS, J. 2008 RANS and hybrid LES/RANS simulation of the effects of micro vortex generators using immersed boundary methods. In *38th Fluid Dyn. Conf. and Ex.*, p. 3728. AIAA.

GIEPMAN, R., SRIVASTAVA, A., SCHRIJER, F.F.J. & VAN OUDHEUSDEN, B.W. 2015 The effects of Mach and Reynolds number on the flow mixing properties of micro-ramp vortex generators in a supersonic boundary layer. In *45th AIAA Fluid Dyn. Conf.*, p. 2779, AIAA.

GIEPMAN, R.H.M., SCHRIJER, F.F.J. & VAN OUDHEUSDEN, B.W. 2014 Flow control of an oblique shock wave reflection with micro-ramp vortex generators: effects of location and size. *Phys. Fluids* **26** (6), 066101.

GIEPMAN, R.H.M., SRIVASTAVA, A., SCHRIJER, F.F.J. & VAN OUDHEUSDEN, B.W. 2016 Mach and Reynolds number effects on the wake properties of microramps. *AIAA J.* **54** (11), 3481–3494.

GRÉBERT, A., BODART, J., JAMME, S. & JOLY, L. 2018 Simulations of shock wave/turbulent boundary layer interaction with upstream micro vortex generators. *Intl J. Heat Fluid Flow* **72**, 73–85.

GRÉBERT, A., JAMME, S., JOLY, L. & BODART, J. 2023 Microramp wake impinging on canonical shock/boundary-layer interaction. *Phys. Fluids* **35** (6), 065144.

JEONG, J. & HUSSAIN, F. 1995 On the identification of a vortex. *J. Fluid Mech.* **285**, 69–94.

JIANG, G.S. & SHU, C.W. 1996 Efficient implementation of weighted ENO schemes. *J. Comput. Phys.* **126** (1), 202–228.

JIMÉNEZ, J., HOYAS, S., SIMENS, M.P. & MIZUNO, Y. 2010 Turbulent boundary layers and channels at moderate Reynolds numbers. *J. Fluid Mech.* **657**, 335–360.

JIMÉNEZ, J. & WRAY, A. 1998 On the characteristics of vortex filaments in isotropic turbulence. *J. Fluid. Mech.* **373**, 255–285.

KONNO, K. & OHMACHI, T. 1998 Ground-motion characteristics estimated from spectral ratio between horizontal and vertical components of microtremor. *Bull. Seismol. Soc. Am.* **88** (1), 228–241.

LEE, S., GOETTKE, M.K., LOTH, E., TINAPPLE, J. & BENEK, J. 2010 Microramps upstream of an oblique-shock/boundary-layer interaction. *AIAA J.* **48** (1), 104–118.

LEE, S. & LOTH, E. 2009 Supersonic boundary-layer interactions with various micro-vortex generator geometries. *Aeronaut. J.* **113** (1149), 683–697.

LI, Q. & LIU, C. 2010 LES for supersonic ramp control flow using MVG at $M = 2.5$ and $Re_\theta = 1440$. In *48th AIAA ASM*, p. 592. AIAA.

LU, F.K., LI, Q. & LIU, C. 2012 Microvortex generators in high-speed flow. *Prog. Aerosp. Sci.* **53**, 30–45.

LU, F.K., PIERCE, A., SHIH, Y., LIU, C. & LI, Q. 2010 Experimental and numerical study of flow topology past micro-vortex generators. In *40th Fluid Dynamics Conf. and Ex.*, p. 4463. AIAA.

LUND, T.S., WU, X. & SQUIRES, K.D. 1998 Generation of turbulent inflow data for spatially-developing boundary layer simulations. *J. Comput. Phys.* **140** (2), 233–258.

MALLAT, S. 1999 *A Wavelet Tour of Signal Processing*. Elsevier.

McCORMICK, D.C. 1993 Shock/boundary-layer interaction control with vortex generators and passive cavity. *AIAA J.* **31** (1), 91–96.

MENEVEAU, C. 1991 Analysis of turbulence in the orthonormal wavelet representation. *J. Fluid Mech.* **232**, 469–520.

PANARAS, A.G. & LU, F.K. 2015 Micro-vortex generators for shock wave/boundary layer interactions. *Prog. Aerosp. Sci.* **74**, 16–47.

PASQUARIELLO, V., HICKEL, S. & ADAMS, N.A. 2017 Unsteady effects of strong shock-wave/boundary-layer interaction at high Reynolds number. *J. Fluid Mech.* **823**, 617–657.

PIPONNIAU, S., DUSSAUGE, J.P., DEBIÈVE, J.F. & DUPONT, P. 2009 A simple model for low-frequency unsteadiness in shock-induced separation. *J. Fluid Mech.* **629**, 87–108.

PIQUET, A., ROUSSEL, O. & HADJADJ, A. 2016 A comparative study of Brinkman penalization and direct-forcing immersed boundary methods for compressible viscous flows. *Comput. Fluids* **136**, 272–284.

PIROZZOLI, S. & BERNARDINI, M. 2011 Turbulence in supersonic boundary layers at moderate Reynolds number. *J. Fluid Mech.* **688**, 120–168.

PIROZZOLI, S., BERNARDINI, M. & GRASSO, F. 2008 Characterization of coherent vortical structures in a supersonic turbulent boundary layer. *J. Fluid Mech.* **613**, 205–231.

PIROZZOLI, S. & GRASSO, F. 2006 Direct numerical simulation of impinging shock wave/turbulent boundary layer interaction at $M = 2.25$. *Phys. Fluids* **18** (6), 065113.

POINSOT, T.J. & LELE, S.K. 1992 Boundary conditions for direct simulations of compressible viscous flows. *J. Comput. Phys.* **101** (1), 104–129.

PRIEBE, S., TU, J.H., ROWLEY, C.W. & MARTÍN, M.P. 2016 Low-frequency dynamics in a shock-induced separated flow. *J. Fluid Mech.* **807**, 441–477.

QUADROS, R. & BERNARDINI, M. 2018 Numerical investigation of transitional shock-wave/boundary-layer interaction in supersonic regime. *AIAA J.* **56** (7), 2712–2724.

SALVADORE, F., MEMMOLO, A., MODESTI, D., DELLA POSTA, G. & BERNARDINI, M. 2023 Direct numerical simulation of a microramp in a high-Reynolds number supersonic turbulent boundary layer. *Phys. Rev. Fluids* **8**, 110508.

SATHYANARAYANA, S., BERNARDINI, M., MODESTI, D., PIROZZOLI, S. & SALVADORE, F. 2023 High-speed turbulent flows towards the exascale: STREAmS-2 porting and performance. *J. Parallel Distrib. Comput.* (submitted). arXiv:2304.05494.

SPALART, P.R., MOSER, R.D. & ROGERS, M.M. 1991 Spectral methods for the Navier–Stokes equations with one infinite and two periodic directions. *J. Comput. Phys.* **96** (2), 297–324.

SUN, D., CHEN, J., LI, C., LIU, P., GUO, Q. & YUAN, X. 2020 On the wake structure of a micro-ramp vortex generator in hypersonic flow. *Phys. Fluids* **32** (12), 126111.

SUN, D., GUO, Q., LI, C. & LIU, P. 2019 Direct numerical simulation of effects of a micro-ramp on a hypersonic shock wave/boundary layer interaction. *Phys. Fluids* **31** (12), 126101.

SUN, Z., SCHRIJER, F.F.J., SCARANO, F. & VAN OUDHEUSDEN, B.W. 2012 The three-dimensional flow organization past a micro-ramp in a supersonic boundary layer. *Phys. Fluids* **24** (5), 055105.

SUN, Z., SCHRIJER, F.F.J., SCARANO, F. & VAN OUDHEUSDEN, B.W. 2014 Decay of the supersonic turbulent wakes from micro-ramps. *Phys. Fluids* **26** (2), 025115.

TAMBE, S., SCHRIJER, F.F.J. & VAN OUDHEUSDEN, B.W. 2021 Relation between geometry and wake characteristics of a supersonic microramp. *AIAA J.* **59** (11), 4501–4513.

TITCHENER, N. & BABINSKY, H. 2015 A review of the use of vortex generators for mitigating shock-induced separation. *Shock Waves* **25**, 473–494.

TORRENCE, C. & COMPO, G.P. 1998 A practical guide to wavelet analysis. *Bull. Am. Meteorol. Soc.* **79** (1), 61–78.

TOUBER, E. & SANDHAM, N.D. 2009 Large-eddy simulation of low-frequency unsteadiness in a turbulent shock-induced separation bubble. *Theor. Comput. Fluid Dyn.* **23**, 79–107.

YAN, Y., CHEN, C., LU, P. & LIU, C. 2013 Study on shock wave-vortex ring interaction by the micro vortex generator controlled ramp flow with turbulent inflow. *Aerosp. Sci. Technol.* **30** (1), 226–231.

YU, M., MODESTI, D. & PIROZZOLI, S. 2023 Direct numerical simulation of flow in open rectangular ducts. *J. Fluid Mech.* **977**, A32.